Processing and interpretation of seismic reflection data from the Los Humeros super-hot geothermal system

Erika Barison [a],[*], Flavio Poletto [a], Gualtiero Böhm [a], Biancamaria Farina [a], Gerardo Carrasco-Núñez [b], Gianluca Norini [c], Guido Giordano [d], Giorgia Pinna [a]

[a] *National Institute of Oceanography and Applied Geophysics - OGS, Borgo Grotta Gigante 42c, 34010 Sgonico, Trieste, Italy*
[b] *Centro de Geociencias, Universidad Nacional Autonoma de Mexico, Campus UNAM Juriquilla, Querétaro, 76230, Mexico*
[c] *Istituto di Geologia Ambientale e Geoingegneria, Consiglio Nazionale delle Ricerche, Milano, Italy*
[d] *Dipartimento di Scienze, Università Roma Tre, Roma, Italy*

ARTICLE INFO

ABSTRACT

The Los Humeros volcanic complex is a geothermal field in Mexico that is now being further investigated as a candidate for the development of a super-hot geothermal system, as it has a temperature of over 350 °C. The European Horizon 2020 project GEMex (2016–2020) worked in this context aiming to characterize the geological and geophysical aspects of the area to assess the feasibility of a super-hot geothermal system. We describe the results of time and depth processing and interpretation of legacy 2D reflection seismic lines acquired in 1998 to study the deep structures of the caldera in the Trans-Mexican Volcanic Belt. The study is relevant for the geophysical characterization of the subsurface in this area, where no vertical seismic profiles are available but only two short sonic well logs. The interpretation of selected seismic horizons in the seismic depth profiles was first determined by the local geological model of the curved caldera and then calibrated by the stratigraphy of the boreholes and the matching of the 2D seismic lines crossing points. The processing outcomes are depth-migrated profiles, the corresponding P-wave velocities and the updated geological models. The main results are the representation of the basement and the identification of the structural make-up of the main units with some of the main faults of the collapsed caldera. Our results provide new insights into the subsurface geometry of volcanic collapses and the geothermal field contained within them at the caldera scale.

1. Introduction

The Los Humeros volcanic complex (LHVC) is an important active geothermal field in the easternmost part of the Trans-Mexican Volcanic Belt (TMVB) in central Mexico, which is the largest active caldera located in the northernmost part of the eastern sector of the Trans-Mexican volcanic belt (Carrasco-Núñez et al., 2017a; Norini et al., 2015, 2019). Los Humeros is one of the oldest geothermal producing fields in Mexico (Arzate et al., 2018), the second after Los Azufres producing electricity in the area of the TMVB (Prol-Ledesma, 1998).

This geothermal field has been exploited since the 1990s (Carrasco-Núñez et al., 2015) and the geothermal power plant has an installed capacity of about 90 MW (Gutiérrez-Negrín, 2019). Recently, new interest has arisen in LHVC because it is now considered a potential candidate for the development of a super-hot geothermal system (Calcagno et al., 2018). A geothermal system is typically defined as super-hot when its temperature is higher than 350° C. Under these

conditions, the fluids have a complex and aggressive geochemical composition that makes it more difficult to extract the geothermal resource (Calcagno et al., 2018).

The H2020 European–Mexican collaboration project GEMex (GEMex, 2016) was carried out to create 2D and 3D geological, geophysical and geochemical models to better define and improve the characterization of this superhot geothermal reservoir (Calcagno et al., 2022) with additional information on the structures at depth, including an enhanced understanding of the recharge mechanism, which is of great importance for the exploitation of this superhot geothermal reservoir. The results are available on GEMex website https://gemex. igg.cnr.it/.

The active seismic can enhance the resolution typically obtained with passive seismic methods (e.g., Toledo et al., 2020 and Granados-Chavarría et al., 2022). Assuming a signal frequency of 20 Hz and velocities from 2400 to 3200 m/s, the expected vertical resolution

of the seismic reflection data (cf. also Eq. (1) in Section 3.4.1) is of the order of 30–40 m. For the same velocities, the lateral resolution of the active seismic before migration ranges between 120-240 m, considering a two-way time (t) of 0.2 and 0.45 s, respectively (Eq. (2) in Section 3.4.1). The goal of migration is to collapse the spatial signal, and to obtain a spatial resolution in the order of half the dominant wavelength of the signal, which can be estimated to be of the order of 50–100 m. Therefore, the additional use of active-seismic data can be highly beneficial for the characterization of deep structures (e.g. Berkhout and Verschuur, 2009 and Gashawbeza et al., 2005). In this paper, we present the results of the processing of legacy active-seismic data performed in the framework of the GEMex project to investigate the deep structures of the Los-Humeros caldera.

Many different geological and geophysical data have been acquired in the area (Arzate et al., 2018). About 60 wells have been drilled (e.g. Carrasco-Núñez et al., 2017a), which supplied lithological, geothermal, geochemical and well-log information. The latter is available for the wells H42, in the depth interval from 1287 to 2206 m, and H43, in the depth interval from 1241 to 1638 m (Figs. 1 and 2). The well data are provided by the Mexican Comisión Federal de Electricidad (CFE).

In addition to the aforementioned geophysical and geological data, legacy active-seismic dataset available for LHVC have been identified and utilized in the framework of the GEMex project. These data consist in four 2D reflection seismic lines (named L2, L3, L4 and L5), acquired by the Compañia Mexicana de Exploraciones S.A. (COMESA) in 1998 with Vibroseis source (COMESA, 1998) for CFE. These sections form a system of crossing lines in the central part of the caldera.

The quality of this active-seismic dataset is challenging due to the irregular field shots coverage in some locations along the seismic lines, to variable S/N in the recorded data and to the strong high-cut frequency filtering of the recording source patterns and receiver arrays. This determines the presence of important directional effects especially in the processing of the shallower data. A relevant work of pre-processing with signal-quality analysis was performed at the National Institute of Oceanography and Applied Geophysics (OGS).

The quality-control analysis was supported by seismic elastic modeling for the interpretation of the wavefields observed in the real shots. This study included a revision of the available geological and geophysical models. We started evaluating the petrophysical model used in Farina et al. (2019), which was derived from the lithological model of Gutiérrez-Negrín and Izquierdo-Montalvo (2010) and the V_P properties derived from the rock cuts provided by the geothermal wells and based on previous works (e.g., Viggiano-G. and Robles, 1988; Contreras et al., 1990). To estimate the shear velocities, they assumed the reference ratio $V_P/V_S = 1.76$ (Lermo et al., 2008). Farina et al. (2019) used a 1D model to analyze the possible effects on the seismic properties of two different heat-transport mechanisms. Afterwards, Poletto et al. (2019) calculated full-waveform synthetic signals based on the 2D geological, velocity and temperature models of Los Humeros (Figs 7, 8 and 9 in Poletto et al., 2019) proposed by Verma et al. (1990).

In the following, we will illustrate the main features and results of the processing of these legacy seismic lines. In the calculations of the elastic signals we have not included temperature effects. The aim is to provide an overview of the active-seismic information for joint evaluation and data integration with other geological and geophysical data collected in the framework of the GEMex project. After an initial processing in the time domain, with a preliminary time–velocity analysis, including inversion of the shallow direct arrivals, the compressional seismic signals have been processed and inverted directly in the depth domain by 2D pre-stack depth migration (PSDM). The initial *P*-waves depth-interval velocity model was set up utilizing literature information and the results from the geological model of the GEMex project (2016, work-package WP3), which includes relevant information about geological formations and faults (Calcagno et al.,

2018) (Fig. 2). The initial model was then updated by subsequent velocity analysis based on seismic coherency methods.

These active-seismic data represent a unique dataset to characterize the geological structures at depth, even at greater depths than those of the wells, which is even more important in the absence of vertical seismic profiles (VSP) in the area.

2. Geological setting

The LHVC is a collapse caldera hosting a geothermal field located in the eastern sector of the TMVB, which is constituted by bimodal volcanism with large stratovolcanoes, calderas, cinder cones, rhyolitic domes and maars (Carrasco-Núñez et al., 2017a and references within). LHVC originated in the Pleistocene and it is mainly a basalt-andesite-rhyolite caldera (Yáñez and García, 1982; Carrasco-Núñez et al., 2017a).

The present caldera complex originated from different eruptive episodes, including two major caldera-forming events. As can be seen in the maps of Fig. 1a and b, this caldera complex is characterized by two partially-preserved ring structures. The external, bigger and older one, the Los Humeros caldera, originated 164.0 ± 4.2 ky ago (Carrasco-Núñez et al., 2018) with the eruption of the 290 km^3 rhyolite Xaltipan ignimbrite (Cavazos-Álvarez and Carrasco-Núñez, 2020). The inner one, comprising Los Potreros caldera, formed 96 ky ago, is associated with the eruption of the 15 km^3 Zaragoza ignimbrite (Carrasco-Núñez and Branney, 2005; Carrasco-Núñez et al., 2018), (Fig. 2).

Between these two main episodes and after them, various eruptive episodes of different eruptive styles (effusive and explosive eruptions) and chemical composition contributed to the evolution of the LHVC (Ferriz and Mahood, 1984); Carrasco-Núñez. A reviewed lithostratigraphic interpretation of the subsurface geology was proposed by Carrasco-Núñez et al. (2017a) for LHVC, subsequently recalled by Calcagno et al. (2018) within the GEMex project. This interpretation considers four principal groups reported in the geological cross section of Fig. 2 and named as follow:

G1 = Post-caldera;
G2 = Caldera volcanism;
G3 = Pre-caldera andesitic volcanism;
G4 = Regional meta-sedimentary basement.

These groups are subdivided into nine lithostratigraphic units (Carrasco-Núñez et al., 2017a; Calcagno et al., 2018; Arzate et al., 2018; Weydt et al., 2021). In the geological analysis of the seismic models, we used both the nine lithostratigraphic units and the new 3D regional and local models provided by Calcagno et al. (2018), as guidelines to interpret the 2D seismic lines and the velocity profiles.

3. Data processing

We focus on the geophysical and geological analysis on the superhot geothermal system of the LHVC (GEMex, 2016). Many studies have been done to characterize and understand the behavior of this geothermal reservoir in terms of geophysics and geology (e.g. Arzate et al., 2018; Carrasco-Núñez et al., 2017a; Urban and Lermo, 2013, 2017; Lermo et al., 2008; Weydt et al., 2021), petrology and volcanology (e.g. (Ferriz and Mahood, 1984; Carrasco-Núñez et al., 2012)), thermal and pressure conditions (e.g., (Deb et al., 2021)). For our analysis, we start from the simplified lithological model of Gutiérrez-Negrín and Izquierdo-Montalvo (2010) and derive the solid and dry-rock properties from literature in addition to the reported average porosity and density (Aragón-Aguilar et al., 2017; García-Estrada, 1992).

The contribution of active seismic data is relevant to provide detailed information on deep seismic structures, to be integrated with the other geological and geophysical measurements in the local model of Los Humeros (Calcagno et al., 2018). Below, we describe the work of reprocessing of the legacy active-seismic data of Los Humeros.
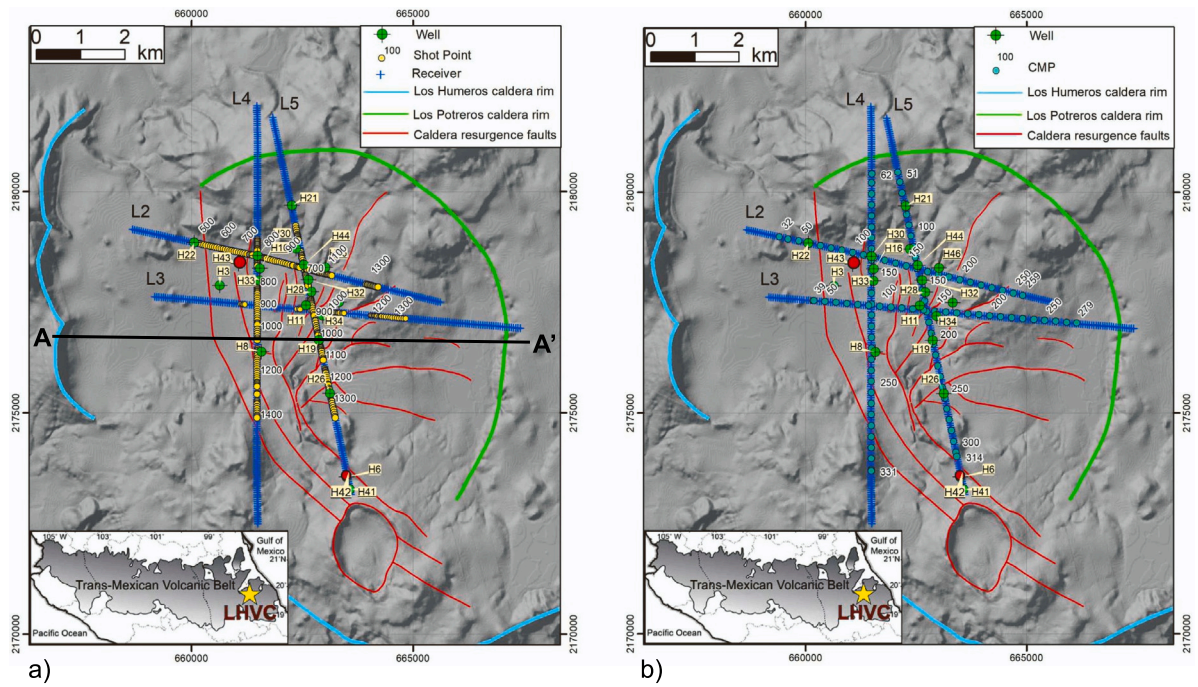
Fig. 1. Location map of the active seismic lines with (a) shot points and receiver positions marked by yellow bullets and crosses, respectively, and (b) CMP (blue bullets) positions in the Los Humeros volcanic complex (LHVC). The location of the wells H42 and H43, for which sonic logs are available, are marked with red bullets. The LHVC fault system is also shown (modified after Calcagno et al., 2018). In the bottom-left corner, the position of the LHVC in the Trans-Mexican volcanic belt is shown by light blue, green and red lines (modified after Arzate et al., 2018). The black line AA' in figure (a) represents the cross section shown in Fig. 2. The coordinate system is WGS84 Zone 14North. (For interpretation of the references to color in this figure legend, the reader is referred to the web version of this article.)
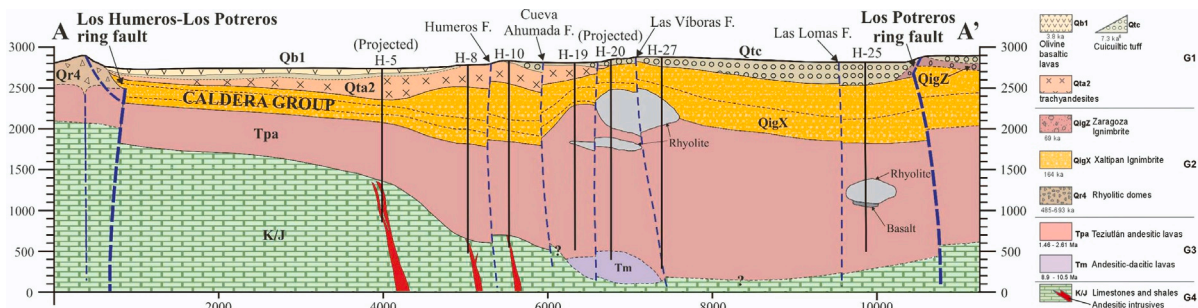
Fig. 2. Schematic geological cross section of the Los Potreros caldera, showing the subsurface geometry of the main stratigraphic units, volcanotectonic structures and geothermal wells. Vertical axis shows elevation in meters above sea level, horizontal axis show distance in meters. The trace of the geological cross-sections is shown in Fig. 1.
Source: Modified from Carrasco-Núñez et al. (2017a).

3.1. Data collection and editing

The purpose of this step was to recover, restore and prepare the relevant active-seismic dataset for the subsequent reprocessing. The raw data have been supplied by Universidad Nacional Autonoma de Mexico (UNAM), with the permission of CFE.

The initial preparation phase required data formatting to SEGY, selection and editing. The legacy dataset consisted partly of already correlated shot points (SP) (5 s length) and partly of non-correlated SPs (21 s length), for the available SP with a variable number of repeated vibrations for every shooting position of each line. Consequently, we completed the process of crosscorrelation of the raw geophone traces with the vibroseis-source sweep, and stacked the correlation results (vertical stack) for each nominal shot point missing in the already-correlated dataset, apart from a few superpositions. While the original correlated and stacked SP files have been provided with an average number of one or two repetitions for each SP position for all the lines — with the only exception of one shooting position with higher number of repetitions —, for the original uncorrelated traces we have from 10 to 12 vibrator-shooting repetitions for the same SP.

The legacy correlated SPs and the SPs were correlated starting from the field signal show signal amplitude variability among the shots of a same line. There was also large amplitude variability in the traces of the individual shot gathers, so, before multichannel signal processing, we balanced the traces within the single shots to mitigate undesired amplitude variation effects.

3.2. Acquisition layout

The reflection-seismic survey consists in four 2D lines acquired in Los Humeros Caldera with Vibroseis source by COMESA, for CFE in 1998:

– L2, with total acquisition length 7145 m;
– L3, with total acquisition length 8293 m;
– L4, with total acquisition length 9444 m;
– L5, with total acquisition length 8695 m,

Fig. 1a shows the location of the seismic lines crossing in the faulted caldera area, with the position of sources and receivers. Table 1
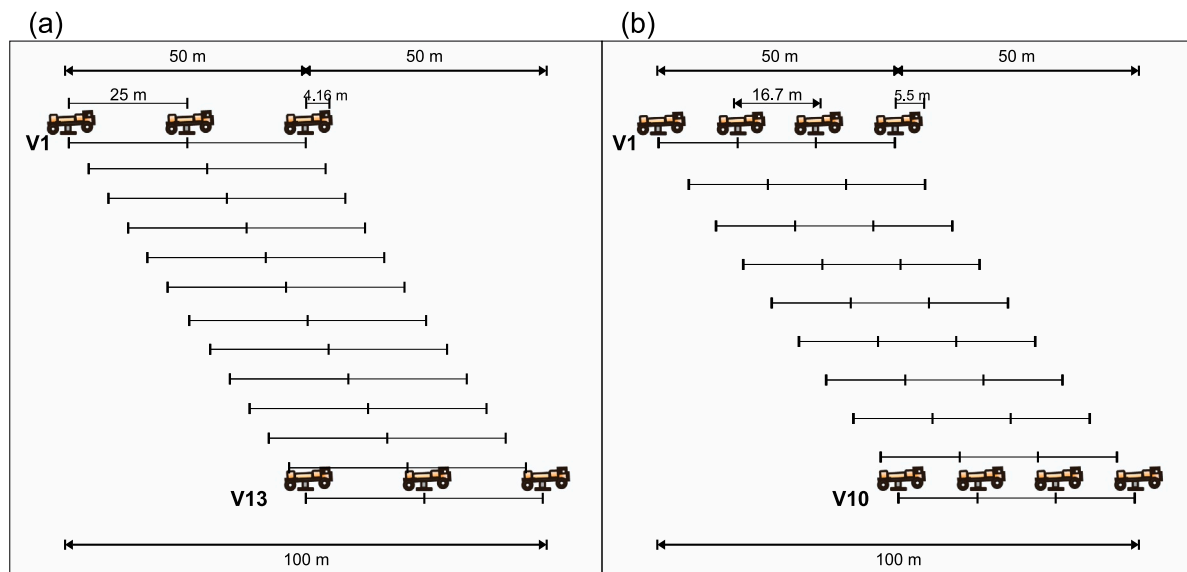
Fig. 3. The two different patterns of vibrations (a) and (b), described in Table 1 (modified after seismic acquisition report; COMESA, 1998).

Table 1
Main acquisition parameters for the Los Humeros active seismic lines.

Parameter	Value
Line length	L2 = 7145 m, L3 = 8293 m, L4 = 9444 m, L5 = 8695 m
Source	Vibroseis
Sample rate	2 ms
Record length	5 s correlated data, 21 s raw-field data
Sweep frequency	12–64 Hz
Sweep parameters	4 Vibrators – 16.7 m – 10 sweeps – 5.5 m (a)
	3 Vibrators – 25 m – 13 sweeps – 4.16 m (b)
	16 + 5 s sweep length
Detection pattern	$N = 24$ elements; $X = 4$ m at constant distance; $L = 92$ m
Receiver spacing	50 m
No. of channels	96
Offset	min = ±300 m, Max = ±2700 m
Spread	Symmetrical split, gap 11 traces
Geo datum	NAD-27 converted to WGS84 Zone 14N
Fold	4800%

summarizes the main acquisition parameters. The vibroseis source has a sweep-frequency bandwidth between 12 and 64 Hz.

The acquisition report provides the specifications of two different source patterns (COMESA, 1998). One pattern consists of 10 moving positions × 4-vibrators-array spaced 16.7 m with a shift of 5.5 m between each block (Fig. 3a), and another of 13 moving positions × 3-vibrators-array, spaced 25 m with a shift of 4.2 m (Fig. 3b), both with a total length of approximately 100 m. This total length is comparable to the length of the receiver detection pattern. However, there are no detailed indications about the distribution of the two acquisition patterns of Fig. 3 within the survey layout. With both these configurations, the pattern directivity effects at sources and receivers are stronger for signals with shorter apparent wavelengths, i.e. higher seismic frequencies and inclined incidence angles. The radiation and directivity properties of the patterns of vibrator sources and response of the geophone receiver array are discussed in detail in Appendix A.

The practical effect is a difficult interpretation of weak high-frequency signals at shallow depths in the seismic data. In addition, the complexity and variability of near-surface conditions over large arrays, although aimed at boosting the weaker reflection signals emerging with vertical travelpaths from depth, can conversely lead to obtaining weaker shallower signals where non-constructive grouping and stacking is achieved. We observed that the source patterns, although attenuating the surface waves, in general, generated poor S/N especially for direct and refracted events at higher frequencies and positions closer to the shot point (short offsets near the gaps).

Moreover, in the field shot records there is a gap of 11 receiver traces (600 m = 2 × 300 m per side) around the central-nominal shooting position to remove the traces with higher noise levels. This gap also deletes information on the shallower layers conveyed by near-offset waves (Barison et al., 2019), as in the raw-field correlated shot shown before filtering and trace balancing in Fig. 4. Low-frequency bandpass filters have been utilized to reduce the high-frequency noise and to improve S/N for the recognition and boosting of deep reflections.

3.3. Time processing

The improvement of S/N in the seismic data is a key aspect in active seismic processing. After having inspected the data shot-by-shot for each line, with the analysis of the amplitude/frequency spectrum transformed in the Fourier frequency domain, we time-processed the data to obtain a starting stack velocity section (Yilmaz, 2001) by using VISTA®2021 - Desktop seismic data processing software.

Fig. 5 shows a scheme of the (a) time- and (b) depth-processing (Section 3.4) flow. In the latter, the yellow boxes evidence the depth-tomography inversion phases (Section 3.4.2).

The four 2D lines have a maximum nominal fold of 4800%, with theoretical 86 SPs for each line and symmetrical split (see the acquisition report shown in Table 1). The raw data we received satisfy these indications only for the line L2. Line L3 has only 53 SP positions, line L4 has 87 SPs, while line L5 has 101 SPs, however 11 of them are off-end SPs. Since we do not have a detailed acquisition SP list (field report) apart from trace header's indications, we decided to use all the records in our possession. Another aspect that influences the final fold distribution is the non-regular distribution of the SP positions along every line in the caldera (Fig. 1a). These variations can be observed in Fig. 6, which shows the CMP fold for each line and highlights the crossing points' position. We note the average poor fold of line L3, of about 30, while L5 fold reaches values of 60. The position map of the CMPs is shown in Fig. 1b. After the calculation of the geometry and of the CMP nominal fold for each line (Fig. 6), we edited the traces to reduce or remove the noisier traces, and applied a 30 Hz Notch filter to
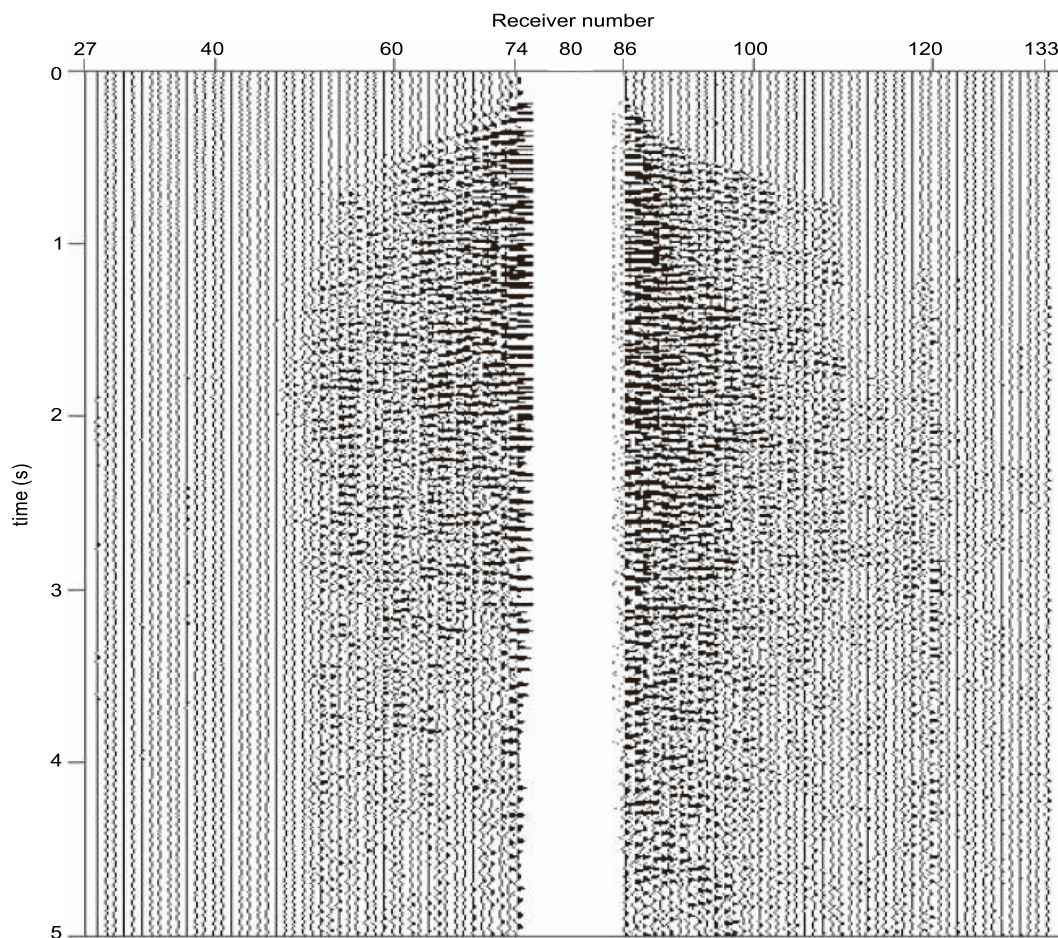
Fig. 4. Example of raw data, crosscorrelated shot, in which the presence of high-amplitude noise at shorter offsets is evident. The horizontal axis shows the receiver numbers for the SP, i.e. the active receivers for this SP are from 27 to 74 and from 86 to 133, with the central gap of eleven traces.

remove a constant harmonic noise present in all the shot gathers, which masks in particular the signals at short-medium times. More examples of the initial conventional time-processing parameters and results are shown in Appendix B.

3.4. Depth processing

We used the Cat3D software for the travel-time tomography (Böhm et al., 2016) (Section 3.4.1) and GeoDepth tools from Paradigm®15 suite to perform the depth processing (par. Sections 3.4.2 and 3.4.3). With GeoDepth it is possible to run a residual depth moveout analysis and a 2D grid-based tomography of depth migrated gathers to improve the depth interval velocity section. This method is also known as the Common Image Gather (CIG) migration analysis.

The main steps in the depth processing flow are the following (Fig. 5b):

– Initial interval depth velocity model;
– Initial Kirchhoff Pre-Stack Depth Migration (PSDM)
– CIG residual analysis;
– 2D grid-based tomography;
– Calculation of the updated depth interval velocity model;
– Kirchhoff Pre-Stack Depth Migration (PSDM): aperture 50 CMP (1250 m);
– Stack by 0.5 power;
– Frequency-space (FX) prediction on migrated sections: trace window 100 traces; time window 100 ms; filter length 9 traces.

3.4.1. First-break travel-time tomography

The directional properties in the source and receiver patterns used for the acquisition focalized the energy on the central traces and downward, so the shallow reflections at large offsets are weak and not easily detectable in the noisy shallow data. This affected the stack velocity analysis at shorter times and, consequently, the velocity models and seismic sections, because the shallow reflections were not detectable. Moreover, the applied 600 m central gap of short offset traces removes information from direct arrivals in the shallower part potentially usable for refraction signal analysis. Therefore, we decided to fill this lack in the shallow velocity information with the velocity resulting from the inversion of the first arrivals (Böhm et al., 2019), which provides precious seismic velocity information for the shallower part, at depths till 700–900 m (Fig. 7).

The 2D models we used for the first break tomography are defined by a regular initial grid of 250 m in X and 60 m in Z. After applying the "stagger grid" method (Vesnaver and Böhm, 2000), the discretization becomes smaller (84 m laterally), while maintaining the same reliability of the grid.

Considering a dominant frequency of 20 Hz for the shallower signals with velocities from 2400 to 3200 m/s, the vertical resolution calculated using the approximated value of $\lambda/4$, according to Ricker's criterion, (Eq. (1)) was estimated to be from 30 to 40 m:

$$\frac{\lambda}{4} = \frac{v}{4f} \tag{1}$$

while the lateral resolution (r), using the Fresnel radius (Eq. (2)):
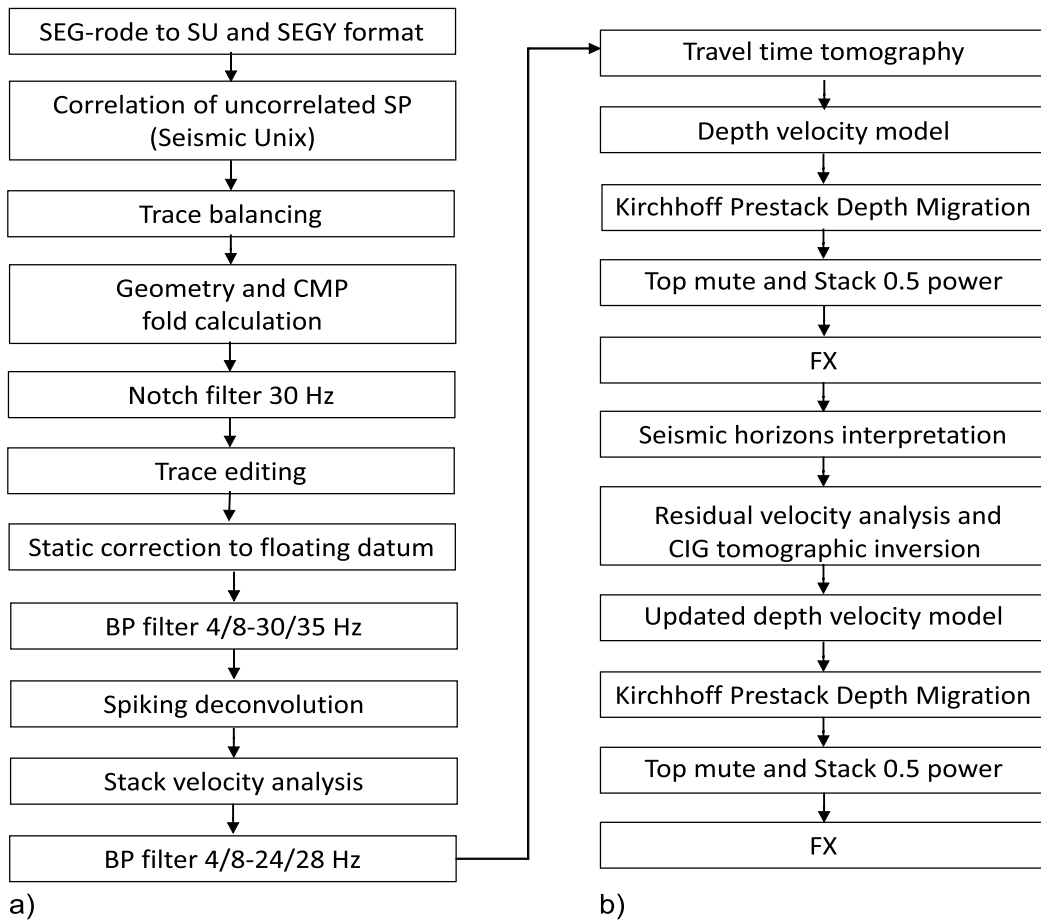
$$r = \frac{v}{2}\sqrt{\frac{t}{f}} \tag{2}$$

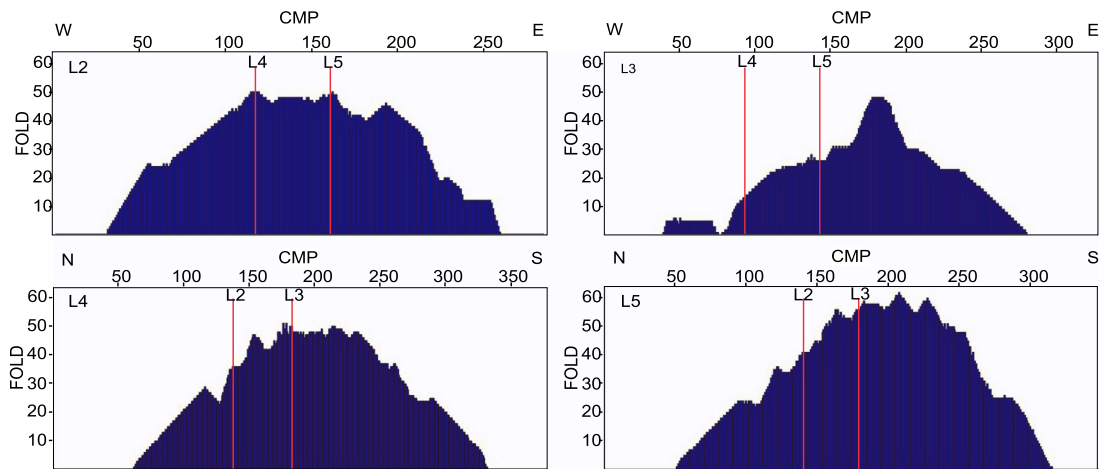**Fig. 5.** (a) Time- and (b) depth- processing flows.

Fig. 6. CMP fold distribution for the four Los Humeros seismic lines, from top left to bottom right in order L2, L3, L4 and L5, respectively. For each fold panel the position of the two crossing sections is indicated by red vertical lines. (For interpretation of the references to color in this figure legend, the reader is referred to the web version of this article.)

where v, t and f are the velocity, the travel time and the dominant signal frequency was calculated to be from 120 to 240 m for the shallower signals at two-way time of 0.2 s and velocity of 2400 m/s and at 0.45 s and velocity of 3200 m/s, respectively.

The knowledge of the near-surface properties both for the correction of traces at the shot and receiver points is important for the subsequent multichannel processing. We calculated the elevation static corrections at the geophones and SP positions to correct the differences in the
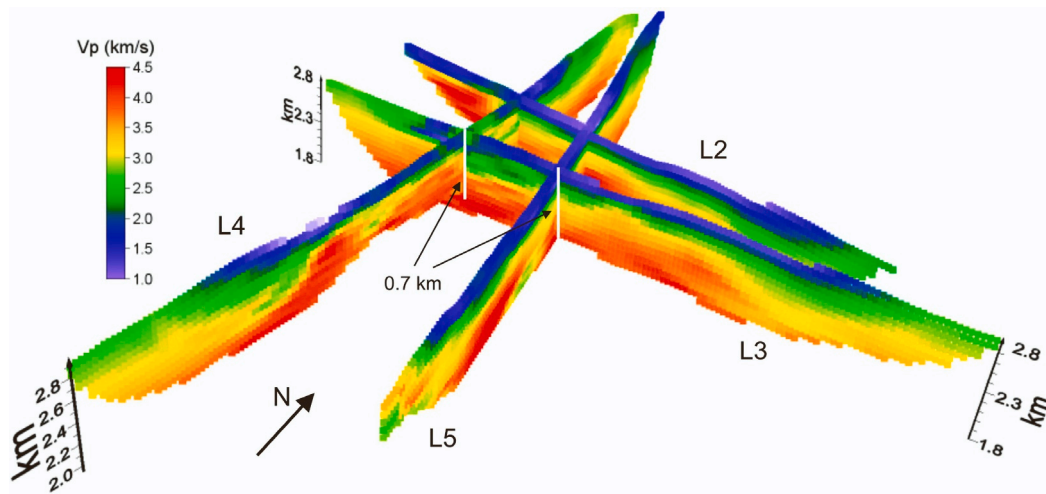
Fig. 7. 3D view of the shallower velocities obtained by the diving-waves travel-time tomography of the 4 active-seismic lines. The vertical scale indicates the elevation above sea level and the maximum investigated depth is 0.7–0.9 km (modified after Böhm et al., 2019).

signal arrival times caused by variations in topography and near-surface formation properties. We computed the elevation static corrections to a floating datum, which approximate the topography using the velocity models obtained from the tomographic inversion of the first-break arrivals picked in the shot gathers for each line (Fig. 7).

To create a depth-interval velocity model for the PSDM of each line, first, we depth-converted the time-stack velocity model, then, replaced the upper values with those resulting from first-break inversion tomography.

3.4.2. CIG tomographic inversion

PSDM requires an accurate depth-interval velocity model to be performed with reliable results, especially in such a complex geological area. The depth-interval velocity models obtained in Section 3.4.1 were used to create the initial PSDM CIGs and sections for each line. When the velocity field is correct, the reflected events in the CIGs are flat in the pre-stack depth domain (Accaino et al., 2005). The degree of non-flatness is a measure of the error in the model. The CIGSs tomography uses this measurement of non-flatness (residual moveout) as input and attempts to find an optimal model, which minimizes the errors.

We used a 2D grid-based tomography consisting of a velocity updating procedure to refine and improve the initial velocity section. The output is an updated velocity model, i.e. the tomography updated velocity section that is a grid-type representation of the model.

3.4.3. Iterative model interpretation

The application of the CIGs tomography velocity analysis requires and is driven by the identification of a horizon-layers model on the 2D depth seismic sections. We performed a residual depth moveout analysis on CIGs to create a residual depth moveout section. This section and the CIGs are the input for the 2D grid-based tomography. The output is an updated velocity section, that we used to run a new PSDM. This interpretative processing was applied to all the four seismic lines of Los Humeros. The analysis was performed separately for each line, however with the constraints of the horizons at the crossing positions. In the analysis of the interval seismic velocities we disregard possible anisotropic effects, which nevertheless are evident in the results of tomographic inversions of shallower seismic data from the active shots, especially in the positions affected by faults (Böhm et al., 2019). This is a key step in the interpretative processing of the depth signals.

We applied a frequency-space (FX) prediction deconvolution (Canales, 1984) on the PSDM stacked section to enhance the laterally-coherent results, then we interpreted the PSDM section, considering as much existing geological and geophysical information as possible. The

geologically-driven interpretation of seismic horizons, together with the analysis of seismic results is described and discussed more in detail in the next sections, with special attention to the identification of robust markers.

Fig. 8 shows, for validation purposes, the comparison between the V_P velocity profiles of the sonic log of the H43 well (available for a limited depth range from 1245 to 1807 m) and of V_P depth interval velocity profiles of lines L2 and L4 obtained in the proximity of the well (Pulido, 2008). In the original log (black line) we can observe a gap with missing data from approximately 1634 m to 1696 m depth. The smoothed log (red line) is calculated using a smoothing window of 30 m. The comparison shows a good agreement between the smoothed log and the velocity curve of L4 (blue line). We observe an agreement among the V_P-velocity trends, with some differences in the velocity profiles of the lines L2 and L4, which cross each other in a faulted area (see the map of Fig. 1, where the position of well H43 is marked by a red spot).

An example of an output depth-velocity model of line L5 is shown in Fig. 9. The shallower part of the model was corrected by the velocities obtained from the shallow tomographic inversion of the diving waves (Böhm et al., 2019), and by tuning the interpretation by comparison of real shot-results and synthetic shots obtained by full-waveform modeling of seismic wavefields using a finite-difference code described in the GEMex deliverable D5.3 (2019) and the input active-seismic model of Fig. 9.

The result shown for a sample shot of line L5 in Fig. 10 demonstrates the consistency of the full-waveform analysis, with appreciable matching of the trends in relevant events in the real and simulated shots. For example the arrows in Fig. 10 point to events, visible in (a) and (b), that can be observed between 0.8 and 1.0 s, around 1.2 s and between 1.2 and 1.4 s. In any case, some differences in the shallower arrivals still persist due to not-yet solved near-surface conditions. The synthetic signals of Fig. 10b were computed by calculating the response of spatial shot- and receiver-arrays with repeated numerical simulations by shifted sources, and stacking the partial results.

To obtain this result, we simulated the synthetic signals of Fig. 10b by calculating the response of spatial shot- and receiver-arrays with repeated numerical simulations by shifted sources, and stacking the partial results. This step was required because the character of the wavefields in the real and synthetic data is not comparable in the absence of a suitable synthetic-pattern compensation. The synthetic responses (signals) were computed using a 2D full-waveform finite difference elastic code (modified after Levander, 1988).
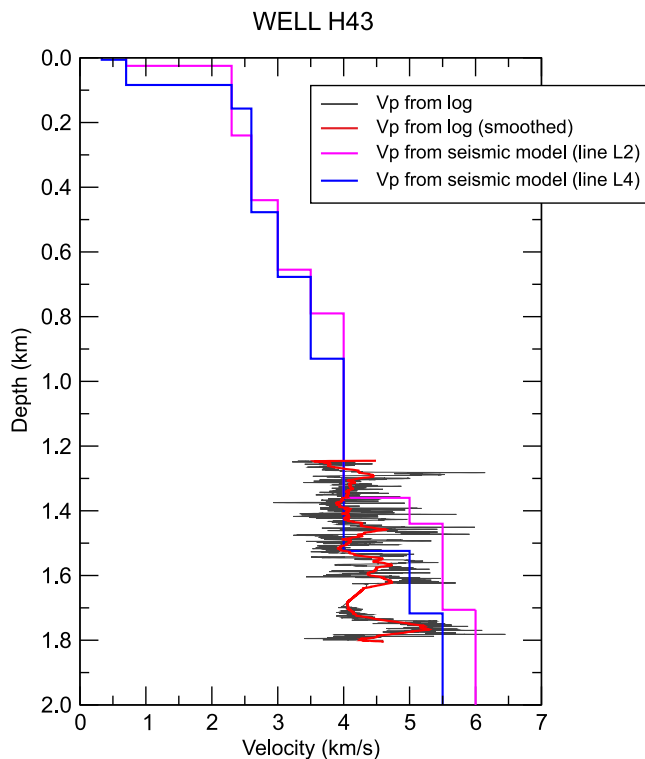
WELL H43

Fig. 8. Comparison of the V_P velocity profiles extracted from the velocity-model of lines L2 and L4 and the available sonic log-interval (from 1245 m to 1807 m depth) in well H43 (ground level elevation 2795 m a.s.l.), located in the proximity of the lines (see Fig. 1 for the line and well position).

We argue that, in the absence of VSP data in the area, this "seismic field experiment" and synthetic model comparison method is an alternative, robust approach, in addition to tomographic velocity analysis, to validate and confirm the depth model in this complex area from the seismic point of view.

4. Interpretative-processing results

After the initial calibration run by the beforementioned iterative approach, we created a new horizon-based depth velocity section, which was used to migrate and interpret again the data. The depth section of the four lines before the interpretation are available as supplementary material in the online version and at gemex.igg.cnr.it/layers/repoigg: geonode:active_seismic_lines. The interpretation is performed on the depth seismic sections, taking into account the geological setting.

4.1. Lithostratigraphic scheme and seismic results

We used the four main lithostratigraphic groups (G1, G2, G3 and G4), listed in Section 2 and shown in the first column of Fig. 11 (from Calcagno et al., 2018), as reference markers for the interpretation of the seismic horizons in the PSDM sections. Whereas, we chose to use the interval velocity of the units, obtained from the seismic data processing and velocity analysis, to define the seismic units from Su1 to Su9 (second column of Fig. 11) because these seismic units can be only tentatively and locally associated with the lithostratigraphic units listed by Calcagno et al. (2018), although with difficult interpretation along the entire seismic sections.

To recognize the marker events in the PSDM sections, we interpreted the seismic results by taking into account the stratigraphic information coming from the wells drilled in the area. In particular we selected twenty wells closer to the lines (whose simplified stratigraphy

are provided as supplementary material), to have more reliable information about the local geological properties in the caldera, where a complex system of faults is present.

The identification of depth of the basement, which is the lowermost boundary of the geothermal reservoir, is the target of main interest, but only eight of the selected wells encountered the basement at variable depths (e.g. Fig. 2). These well constraints enabled us to calibrate this horizon and to better define the faulted geometry of the basement on the seismic lines. This horizon-marker information was of great importance to calibrate the interpretation at depth along the individual sections (GEMex deliverable D8.4, 2020), and subsequently also to extend the joint-interpretation of the horizons to the other lines. Fig. 12 shows the 3D view of the four crossing lines, from the perspective of the L3-L5 crossing position.

Below the basement and maximum well depths the structural information comes from the seismic data by means of the CIG analysis, which provides a velocity model of the deep structures with images of deeper layers below about 4 km from surface, where some horizons can be tentatively interpreted.

The seismic section results and velocity models are shown in the figures from Figs. 13 to 16, (a) and (b), respectively. The horizons interpreted in the sections and in the velocity models correspond to the bottom of the units. The interpreted depth-seismic sections of Figs. 13a, 14a, 15a and 16a also show the stratigraphic profiles of the wells used for geological interpretation.

In this analysis, we defined as "on the line" the wells in the range of 50 m from the line (indicated by black arrows in the Figs. 13a, 14a, 15a and 16a), and as "the wells in the proximity of the line" (indicated by blank arrows in the same figures) those present in the range of 150 m from the line. In the latter, the correspondence in depth between the well stratigraphy and the seismic horizons fits only partially. However, the well selection and choice for interpretation was made case by case, depending on the local conditions and presence of faults, as for well H43, located at 260 m from L2 and 490 m from L4, but relevant because of the presence of the sonic log, and for well H20 and H63 at 220 m and 560 m from the line L3, respectively, which have been considered anyway because we did not have enough wells at shorter distances for the interpretation of this line.

4.2. Main observations

This information together with the in-depth results of the four seismic lines allowed us to obtain a reliable set of images of the LHVC structure with the four main groups: the post-Caldera — G1 (subdivided in Su1 and Su2), the Caldera — G2 (subdivided in Su3, Su4 and Su5), the pre-Caldera — G3 (subdivided in Su6, Su7 and Su8) and the basement — G4 (corresponding to Su9).

As expected from literature (e.g. Ferriz and Mahood, 1984; Carrasco-Núñez et al., 2018), an overall observation of the four seismic lines reveals a global deepening of all the horizons toward the center of the caldera, where the basement reaches the minimum elevation of 100 m a.s.l. (Figs. 14a and 16a).

In general, the basement is shallower to the west and northwest. At the north-western inner rim of the caldera, the basement rises to about 650–1100 m a.s.l., as seen in seismic lines L2 (CMP from 65 to 130), (Fig. 13a) and L3 (CMP from 50 to 140) (Fig. 14a). On the western outer rim of the caldera the basement is even higher, reaching 1700 m a.s.l., as in well H22, which is in line with CMP 59 of L2 (Fig. 13a). Here, the layers are thinner than in the other portions of the profiles, where the caldera collapses allowed the deposition of a considerable volume of pyroclastic, lava and volcanoclastic material. Within the caledera, the pre-caldera group reaches a thickness of more than 1000 m in the central portion of lines L4 (Fig. 15a) and L5 (Fig. 16a). With variable thickness of the inner layers, the caldera group varies from 500–600 m at the edges of the lines to about 900–1000 m in the middle of the sections. Near line L5, well H28 is located in line with CMP 162 and has
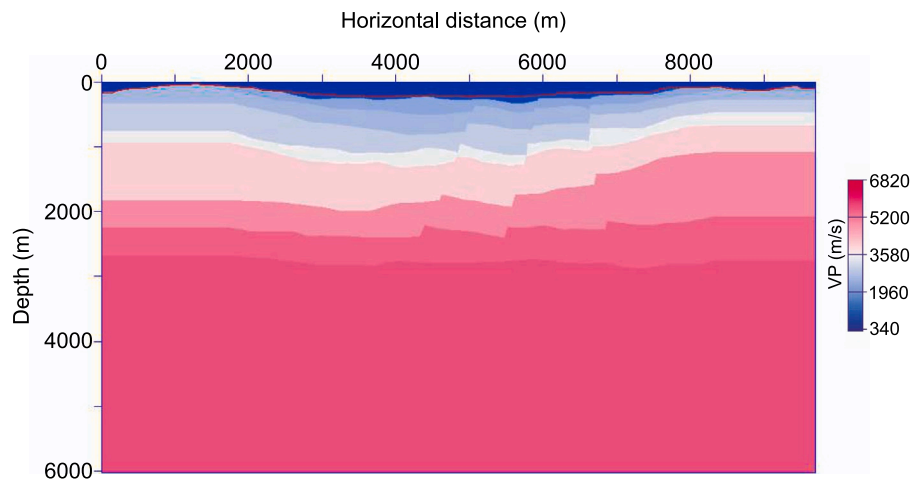
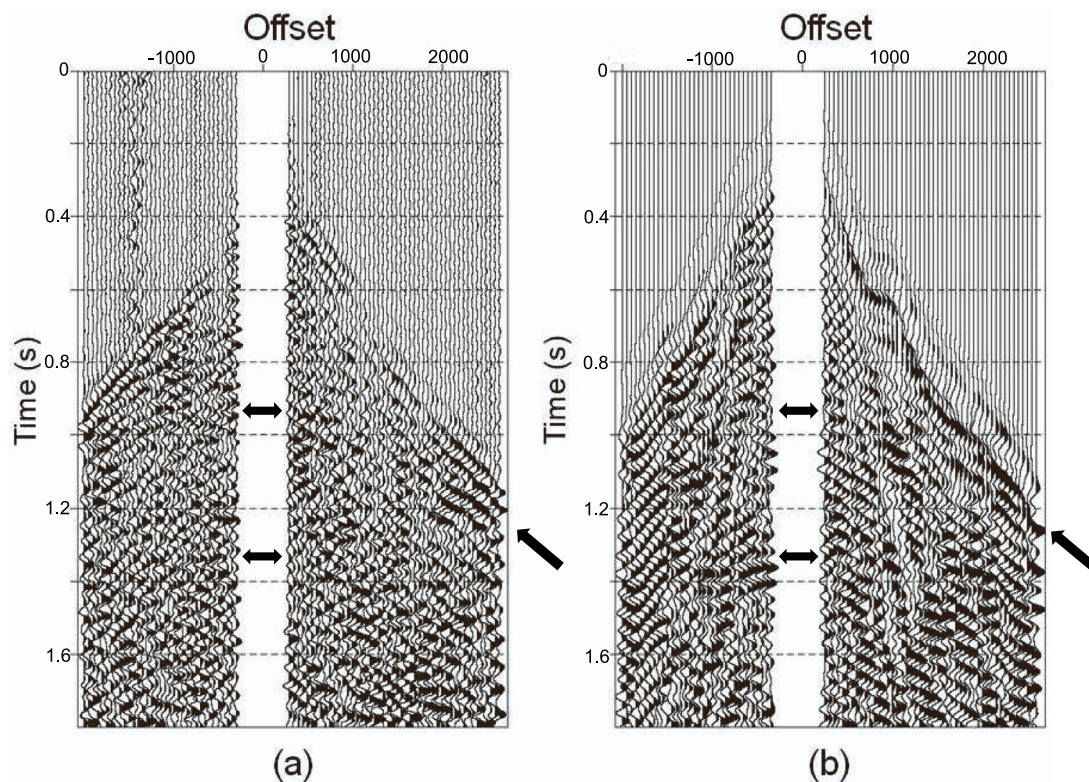**Fig. 9.** Active seismic depth velocity model of line L5.

Fig. 10. (a) Real seismic shot of L5 and (b) full-waveform synthetic signal for the active seismic model of line L5 of Fig. 9. The arrows show significant events, that are present in both images.

a total depth of 2570 m from the surface and encounters the basement at a depth of about 2540–2550 m, which corresponds to an elevation of 200 m a.s.l. The well H26 is located in correspondence of the CMP 256 and has a total depth of 2540 m. This last well did not reach the basement, but it was used to estimate the structural setting compared to well H28. These two wells are 2300 m apart (see Fig. 1). This separation allows to confirm the trend of the subsurface structures, and the deepening of the basement towards the South-East, which finds a correspondence in L5 PSDM profile (Fig. 16a).

At the top of this sequence we find the post-Caldera deposits, which are much thinner (about 200 m or less) compared to the previous ones. These deposits vary in thickness and consist mainly of incoherent material. In particular, this characteristic is valid for Su1, a thin low

velocity (700 m/s) superficial layer that we have identified by diving-wave traveltime tomographic inversion of direct arrivals (Fig. 7), with an average thickness of about 100 m. This layer can be observed in the velocity models of Figs. 13b, 14b, 15b, and 16b.

The overall data quality in terms of S/N is not sufficient for the global reconstruction and imaging of detailed stratigraphic features, including those related to the possible effects due to the presence of fluids and temperature and small displacements along individual fault surfaces. For this reason, we have not investigated in detail the possible presence of specific intrusions. However, the reconstructed fault geometries and associated displacement will be discussed within the frame of the current knowledge, which includes the polyphased caldera collapse development and the similarly polyphased history of caldera resurgence, as discussed in the interpretative geological profiles

Group	Seismic Unit	Interval velocity (m\s)
G1 Post-caldera	Su1	700
	Su2	2300
G2 Caldera	Su3	2600
	Su4	3000
	Su5	3500
G3 Pre-caldera	Su6	4000
	Su7	5000
	Su8	5500
G4 Basement	Su9	6000

Fig. 11. Illustrative scheme of the four main groups, the seismic units and related interval velocities, used for the seismic processing and images interpretation (modified after Calcagno et al., 2018).

of Carrasco-Núñez et al. (2017b), the GEMex Report D3.2 (GEMex, 2019-2020), and recent works by Norini et al. (2019), Lucci et al. (2020), Urbani et al. (2020), Norini and Groppelli (2020), Bonini et al. (2021).

5. Discussions and conclusions

Our study presents the seismic characterization of the inner part of the Los Humeros caldera that we performed within EU H2020 GEMex project through the processing of legacy active-seismic reflection data acquired in 1998. First, we carried out a time processing to improve S/N and obtain an accurate pre-stack seismic dataset together with an initial velocity model. We then moved on to a depth imaging through an iterative process to refine and improve the depth interval velocity model and run the final PSDM. The results we obtained allowed defining the main stratigraphic groups of the Los Humeros caldera system, and the related interval velocity (V_P) resulting from the depth inversion

(Fig. 11). To better identify the geological structure, we calibrate the seismic horizons with the punctual information from the stratigraphy of the drilled wells (GEMex deliverable D5.3, 2019).

As reported in par. Section 3.4.3 there are only two well logs, one of well H43, located close the crossing point between L2 and L4 (Figs. 1 and 8), with a depth range from 1245 to 1807 m, and one of well H42 with a length of approximately of 1 km, but located at the southern edge of L5 (Fig. 1) outside the CMP line and separated by a fault from the line. So this well log was not considered. In addition, there are no VSP data in the studied area, which could have improved the interpretation and calibration with punctual check-shot information. Due to this lack of borehole data, we could not perform the standard procedure of seismic-well tie to boost our interpretation, which has been driven by the wells stratigraphy and the seismic data. The unavailability of standard well-tie data may produce a possible flaw in our interpretation approach.

Moreover, the combination of the initial poor S/N ratio in the seismic lines with the geological complexity of the faulted area makes it difficult to achieve a detailed geological/structural interpretation of local/small volcanic structures, faults and magmatic intrusions (Urbani et al., 2020; Norini and Groppelli, 2020; Lucci et al., 2020; Bonini et al., 2021; Urbani et al., 2021).

From a geophysical-geologically oriented point of view, this procedure enabled us to design the inner structure of the LHVC, recognizing the four main groups through the identification of the marker events along the seismic profiles. The top of the meta-sedimentary basement proved the most difficult marker to constrain because only few wells intercept the basement. However, by combining the well data with the information coming from the lines' crossing points, we were able to recognize the seismic horizon corresponding to the top of the basement.

We distinguished some subdivision inside these groups, based on the variation of the interval velocity. Namely, there are the two seismic units of the post-caldera deposits, with the very low velocity of the first unit (Su1) estimated by shallow seismic data, and the caldera volcanism subdivided in to three seismic units, that are fragmented by
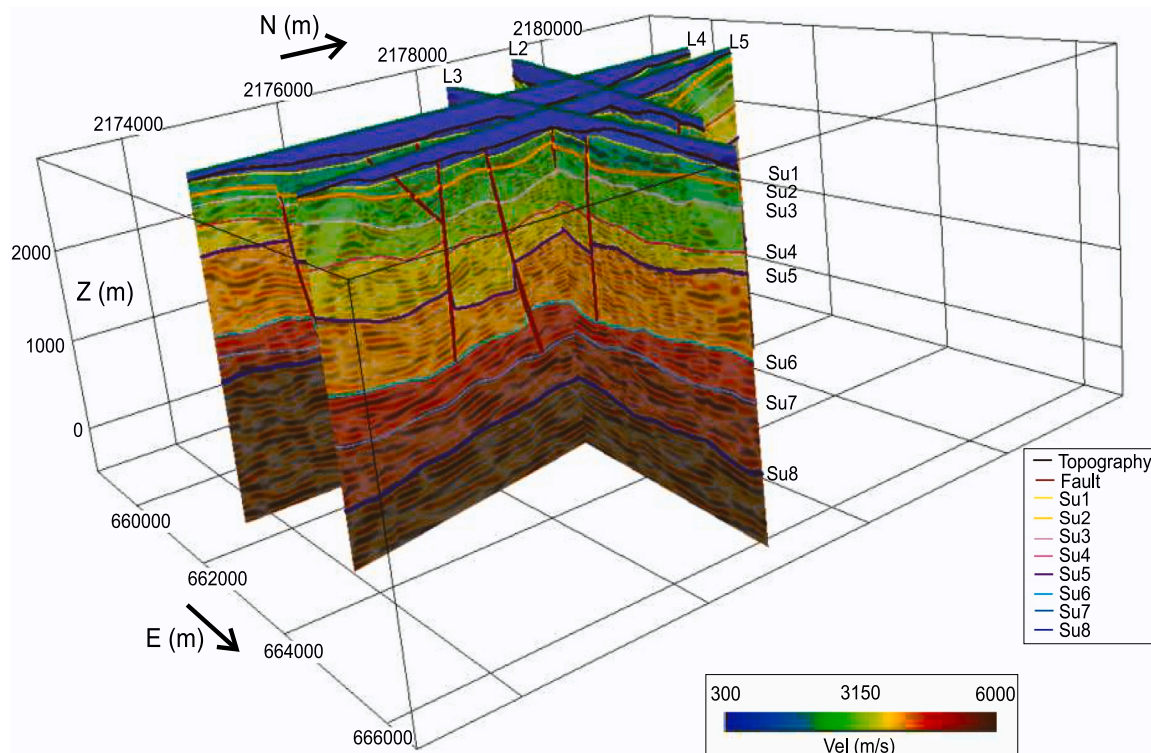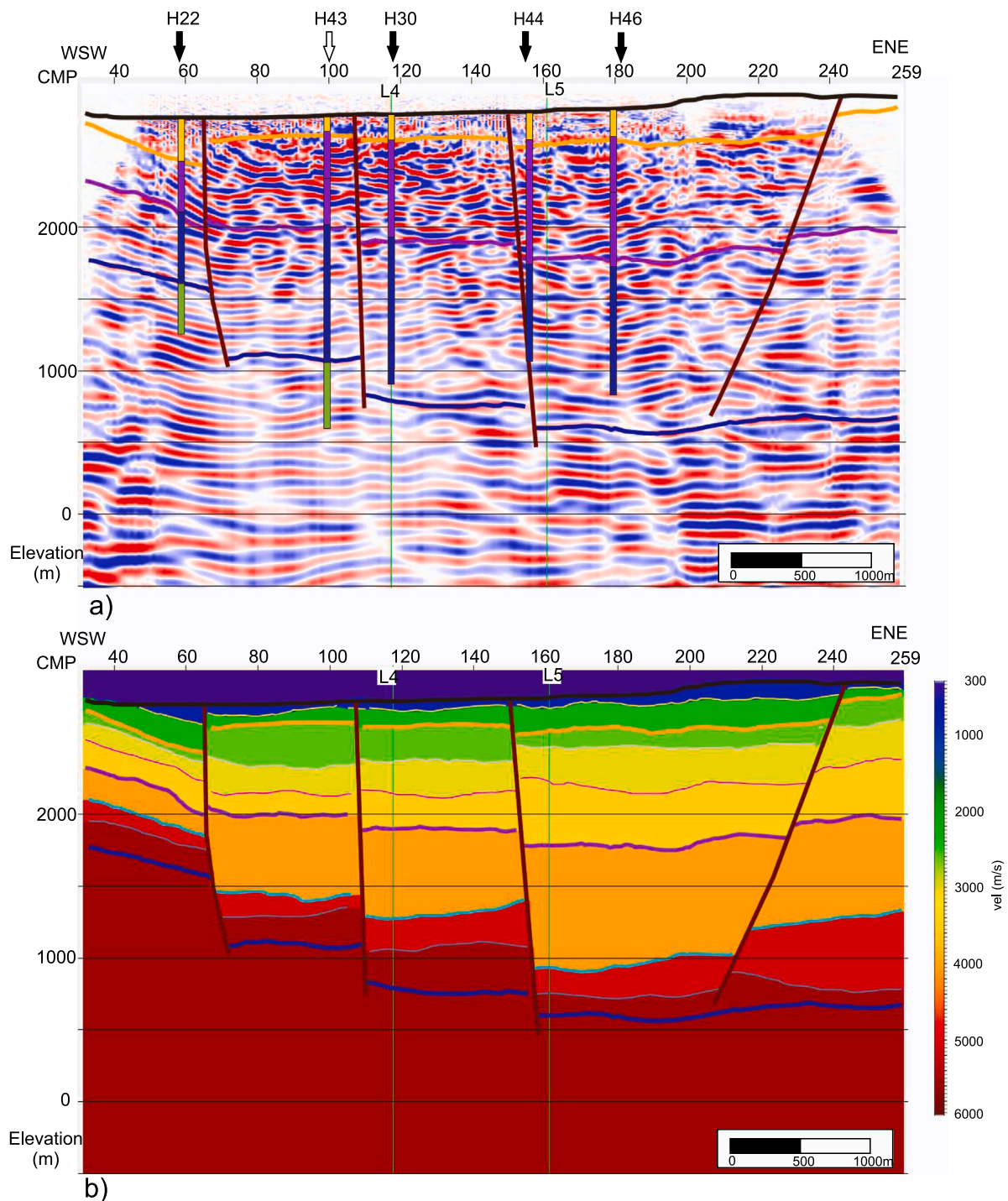

Fig. 12. Detail with 3D view of the Los Humeros 2D crossing lines, depth velocity model and interpretation. The color interpretation of the horizons refers to Fig. 11.
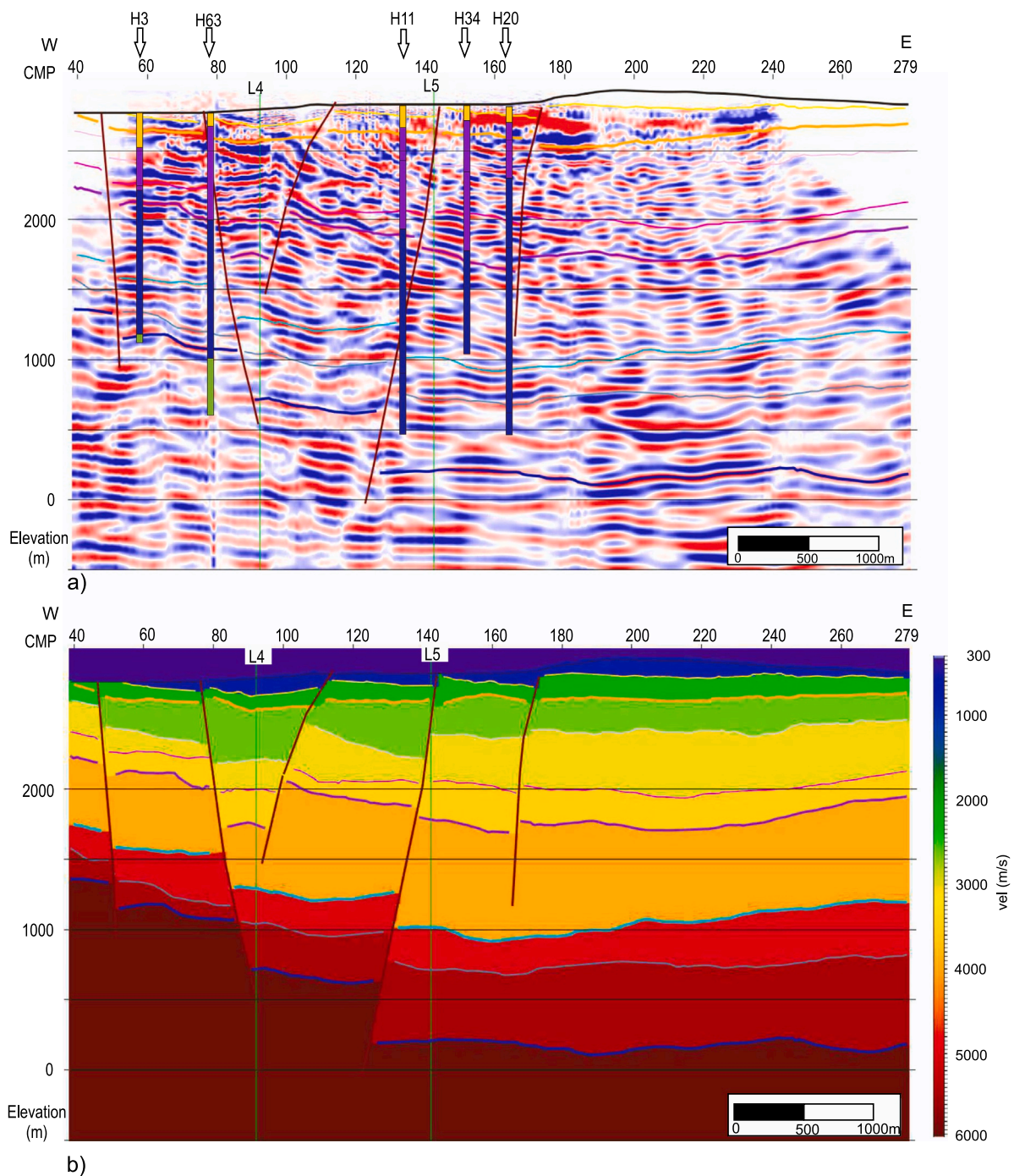
Fig. 13. (a) L2 interpreted depth seismic section with stratigraphic profiles of the used wells. The black arrows indicate wells on the line, the blank arrows indicate wells in the proximity of the line. For the color legend of the horizons and the well stratigraphy see the column "Group" in Fig. 11. (b) 2D depth interval velocity field for line L2. The color legend of the horizons lines is shown in the column "Seismic unit" in Fig. 11. Both in (a) and (b), the green vertical lines indicate the crossing positions with the other lines, the vertical scale is in meters above sea level. (For interpretation of the references to color in this figure legend, the reader is referred to the web version of this article.)

the collapse of the caldera itself. Similar consideration can be made for the three pre-caldera seismic units, which are extended by lateral seismic interpretation to obtain the domains used for depth-seismic inversion purposes.

All lines L2, L3, L4 and L5 (Figs. 13a, 14a, 15a and 16a, and the corresponding velocity sections Figs. 13b, 14b, 15b and 16b) show inversions of fault displacement along their inferred traces, which can bear some volcanological significance. For example, line L2 (Fig. 13a) suggest the presence of normal faults likely associated with caldera

faults, which displace the basement by hundreds of meters with their shallow sections related to minor but consistent reverse displacement of the post-caldera sequence. These may be associated with shallow intrusions, above or within the caldera sequence. Lines L3, L4 and L5 (Figs. 14a, 15a and 16a, respectively) indicate, by contrast, reverse displacement of the basement and normal displacement along the shallow traces of the same faults, suggesting that resurgence associated with deeper intrusions may have waned or ceased over time in some sectors of the caldera.

Fig. 14. (a) L3 interpreted depth seismic section with stratigraphic profiles of the used wells. The blank arrows indicate wells in the proximity of the line. For the color legend of the horizons and the well stratigraphy see the column "Group" in Fig. 11. (b) 2D depth interval velocity field for line L3. The color legend of the horizons lines is shown in the column "Seismic unit" in Fig. 11. Both in (a) and (b), the green vertical lines indicate the crossing positions with the other lines, the vertical scale is in meters above sea level. (For interpretation of the references to color in this figure legend, the reader is referred to the web version of this article.)

From a methodological point of view, the comprehensive study performed by different approaches, demonstrates and confirms the importance of active-seismic data for a detailed at-seismic-scale geophysical recognition of the deep structures in volcanic areas. A direct comparison of the active seismic results with those of the passive seismic methods used in this area is confirmed on average but without details, because of the different resolutions of these methods.

Notwithstanding the complexity of the investigation in the area, the study demonstrates and confirms the importance of active-seismic data for geophysical recognition of the deep structures in volcanic areas and for the stratigraphic interpretation of the geothermal system. This is even more true in the absence of VSP and with limited log information as in the study area.

The reconstruction of the 3D deep geometry of the volcanotectonic faults that accommodated both the caldera collapse episodes and the resurgence episodes is essential in the framework of geothermal exploration as such structures provide the main pathways for the circulation of geothermal fluids. This is specifically true at Los Humeros, where so far the main productive volumes are well known to be controlled by faults (Norini et al., 2019).

Our considerations are that further updates, by iterative interpretation with the integration of results from other geophysical methods and
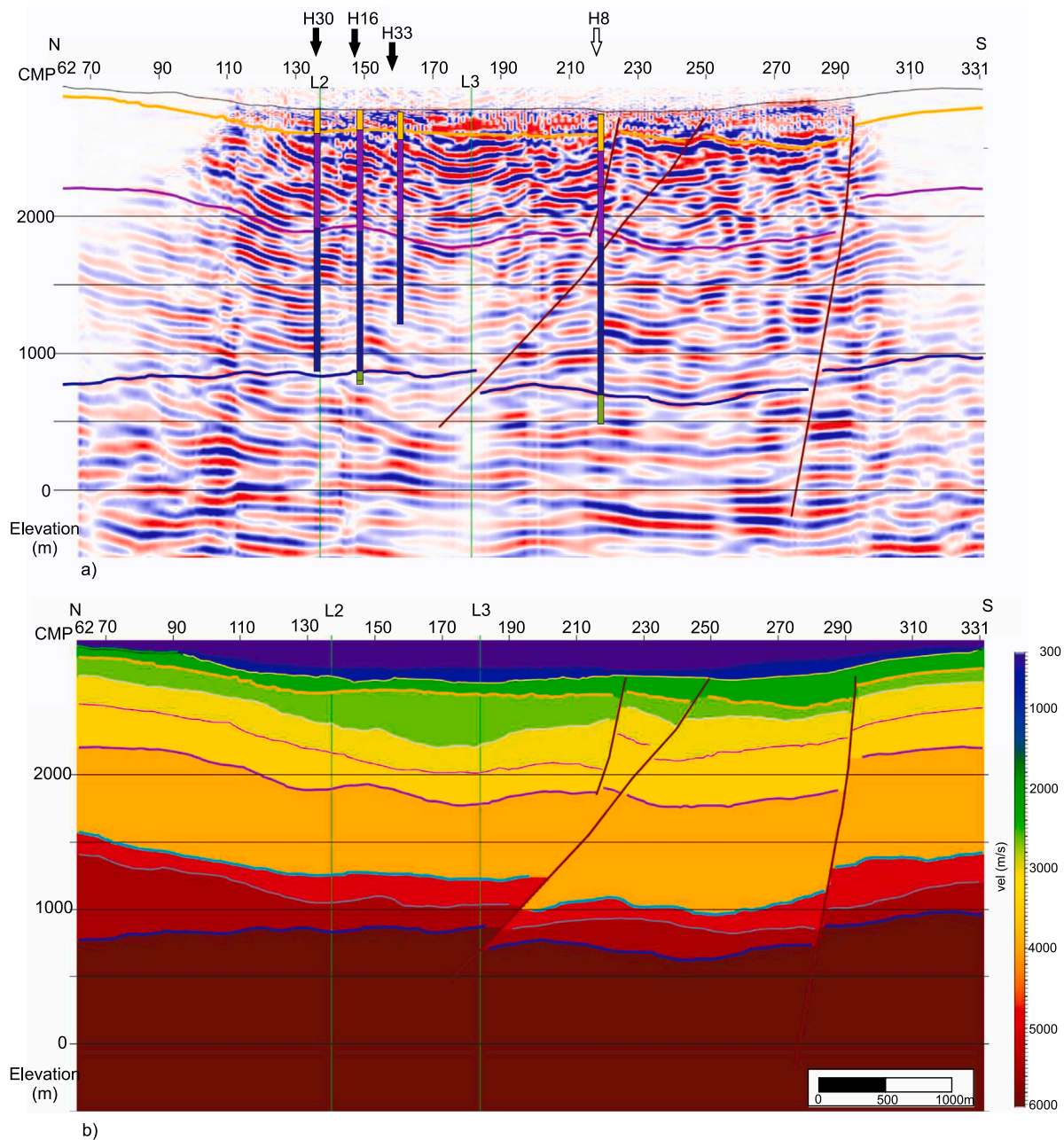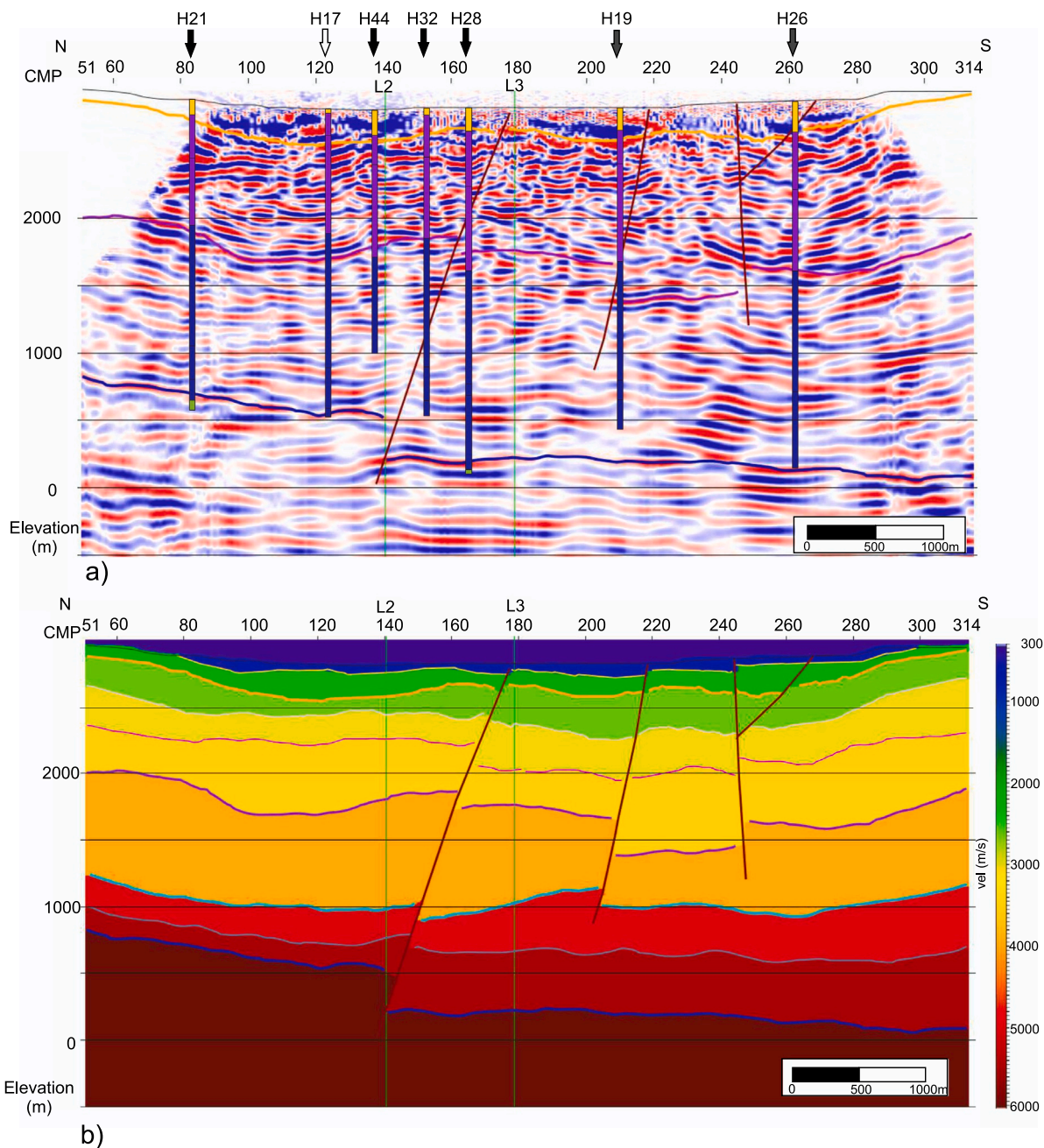
Fig. 15. (a) L4 interpreted depth seismic section with stratigraphic profiles of the used wells. The black arrows indicate wells on the line, the blank arrows indicate wells in the proximity of the line. For the color legend of the horizons and the well stratigraphy see the column "Group" in Fig. 11. (b) 2D depth interval velocity field for line L4. The color legend of the horizons lines is shown in the column "Seismic unit" in Fig. 11. Both in (a) and (b), the green vertical lines indicate the crossing positions with the other lines, the vertical scale is in meters above sea level. (For interpretation of the references to color in this figure legend, the reader is referred to the web version of this article.)

from other geological information, will be beneficial for a revision of the structural setting of the area.

This study is intended as a contribution for the development and exploitation of the geothermal high-enthalpy reservoir. A future confirmation of this preliminary interpretative hypothesis could be an important outcome. Further seismic-depth model calibration could be reached and verified through new geophysical prospecting based on VSP and well sonic and geological logs, for having more detailed and reliable velocity information both to gain better seismic images and to calibrate their interpretation to reduce the potential flaw discussed before in further studies. However, this task is limited by the depth of the wells and by the availability of suitable technology enabling to perform borehole measurements with high-temperature conditions, such as seismic while drilling (e.g., Bakulin et al., 2020) and fiber optic

distributed acoustic sensing (DAS) for its high temperature tolerance (Willis, 2022). Extensive use of a large number of surface seismic wireless point-sensors and sources with adaptable 2D and 3D geometry is envisaged as a future technological development (Bakulin et al., 2018). This solution would enable to achieve improved signal focusing, to boost S/N by supergrouping, and overcome the limitations off the dataset analyzed in this paper, where the strong directional effects of the source and receiver arrays introduce limitations for the imaging of complex dipping structures Appendix A.

The analysis provides data that can be revised jointly with and in the light of any new depth information collected for the site development. By this we intend mainly calibration well seismic and sonic data, as well as new surface seismic campaigns performed with large number of point sensors enabling to steer the signal directionally in the complex

Fig. 16. (a) L5 interpreted depth seismic section with stratigraphic profiles of the used wells. The black arrows indicate wells on the line, the blank arrows indicate wells in the proximity of the line. (b) 2D depth interval velocity field for line L5. The color legend of the horizons is shown in the column "Seismic unit" in Fig. 11. Both in (a) and (b), the green vertical lines indicate the crossing positions with the other lines, the vertical scale is in meters above sea level. (For interpretation of the references to color in this figure legend, the reader is referred to the web version of this article.)

area, in 2D or better 3D. This development is beyond of the scopes of this paper focused on the recovery of legacy data.

CRediT authorship contribution statement

Erika Barison: Conceptualization, Methodology, Formal analysis, Methodology, Writing – original draft, Writing – review & editing , Visualization. **Flavio Poletto:** Conceptualization, Methodology, Formal analysis, Methodology, Resources, Writing – original draft, Writing – review & editing, Project administration, Supervision. **Gualtiero Böhm:** Formal analysis, Methodology, Review & editing. **Biancamaria Farina:** Formal analysis, Methodology, Visualization, Investigation, Review & editing. **Gerardo Carrasco-Núñez:** Investigation, Writing – review & editing. **Gianluca Norini:** Investigation, Writing – review & editing.

Guido Giordano: Investigation, Writing – review & editing. **Giorgia Pinna:** Data curation, Investigation.

Declaration of competing interest

The authors declare that they have no known competing financial interests or personal relationships that could have appeared to influence the work reported in this paper.

Data availability

In case of request of the data, authors have to ask permission to the data owner, because this is a legacy dataset.

Acknowledgments

Appendix A. Array response analysis

We assume plane waves in the far-field approximation for the calculation of the array responses for both the receiver and source configurations, invoking reciprocity. The geometry with a harmonic plane waves sampled by the arrays is shown in Fig. A.1. An incoming (or outcoming) wave with wavefront W is sampled along the array at the surface. N is the number of the sampling points, receivers or sources, in the array, and Δx is the receiver (or source) spacing. The wave is incident (or radiated) with angle α, which is the angle between the wavefront and the surface, equal to the angle between the ray normal to the wavefront and the vertical axis. The angle $\alpha = 0$ corresponds to vertical wave propagation; f and V are the wave frequency and propagation velocity, respectively. At the surface, the signal with apparent wavelength $\lambda_a = (V/f) sin\alpha^{-1}$ is sampled along the array. For the calculation of the array responses obtained with sampling points with variable positive weights $w(i)$ (function of the array index $i = 1, \ldots, N$), as those obtained by multiple vibrations repeated in the same shot point, we use a numerical approach.

The numerical response at the center of an array is calculated by the summation of the phase-shifted harmonic signals as

$$R = \sum_{i=1}^{N} w(i) \cos[2\pi(\Delta x / \lambda_a)(i - i_c)], \tag{A.1}$$

where the phase shifts are calculated for incremental point positions and i_c is the central-point index. Eq. (A.1) can be reformulated as

$$R = \sum_{i=1}^{N} w(i) \cos[\eta(i - i_c)], \tag{A.2}$$

where $\eta = 2\pi\Delta x(f/V)sin\alpha$. From Eq. (A.2) we obtain the normalized numerical response

$$RN = \left| \frac{R}{\max(R)} \right|. \tag{A.3}$$

Examples of response and radiation curves are shown by normalized plots in Fig. A.2. The numerical curves are calculated by the weighted sum of harmonic components (Eq. (A.2)), using the layout of the geophone array (Table 1), and those of the vibrators arrays shown in Fig. 3. For the geophone array we used unit weights $w(i) = 1$ for $i = 1, \ldots, N$. The weights of the vibrator arrays were calculated from the superposition schemes of Fig. 3, neglecting possible mutual impedance effects between vibrators of the same blocks (e.g., Cassand and Lavergne, 1971; Brune et al., 2013) used with these configurations. These calculations do not take into account the directional properties of the source (vertical vibrators) and of the single receiver (geophone vertical component).

In the schematic examples of Fig. A.2 the numerical response/radiation curves are analyzed for harmonic components of different frequencies. The array shifts at the sampling positions i for different ray (incidence and emission) angles are calculated assuming a homogeneous 2000 m/s velocity model. To test the numerical results, we compare the response of a linear geophone array calculated using the analytic function (e.g., Geldart and Sheriff, 2004)

$$RA = \frac{\sin(N\eta/2)}{N \sin(\eta/2)}. \tag{A.4}$$

Fig. A.2a compares the normalized responses represented by polar plots in 2D of the geophone and vibrators patterns associated with the vibrator arrays (a) and (b) of Fig. 3 at a harmonic frequency of 24 Hz. The curves of the vibrator arrays labeled VIB A (Fig. 3a) and VIB B (Fig. 3b) are similar, with minimal differences for their different secondary lobes and smoothing properties. These curves show a moderate difference with the curve of the geophone array at frequency 24 Hz. Fig. A.2b shows the geophone polar diagrams calculated at different frequencies, which confirm the different attenuation effects for non-near-vertical signals at seismic frequencies of 12 (low), 24 (medium) and 48 Hz (higher attenuation). Fig. A.2c shows the numerical radiation curves versus angles for the signals of Fig. A.2a, compared to the analytic geophone curve calculated with the theoretical analytic Eq. (A.4). The numerical response closely matches the analytical one. These effects are important both for receivers and sources.

Finally, in the source-receiver acquisition geometry, we note that the recorded seismic signals are filtered by the composed responses of both the source and receiver arrays. Assuming equal source emission and receiver incidence angles as an approximation, Fig. A.2d compares
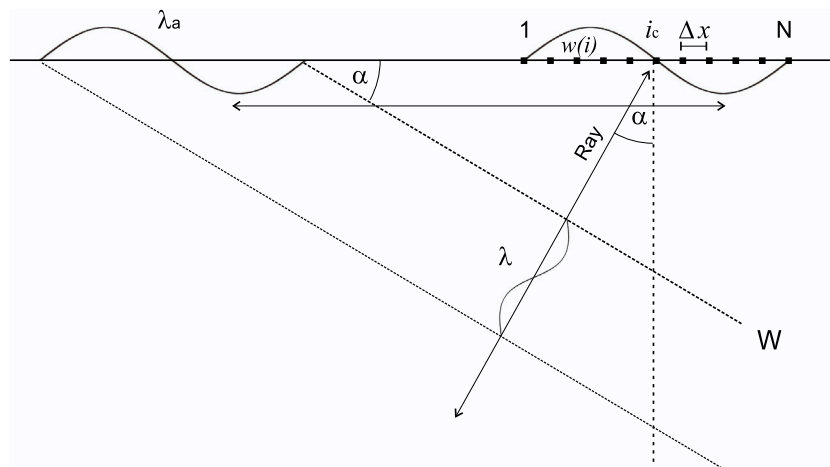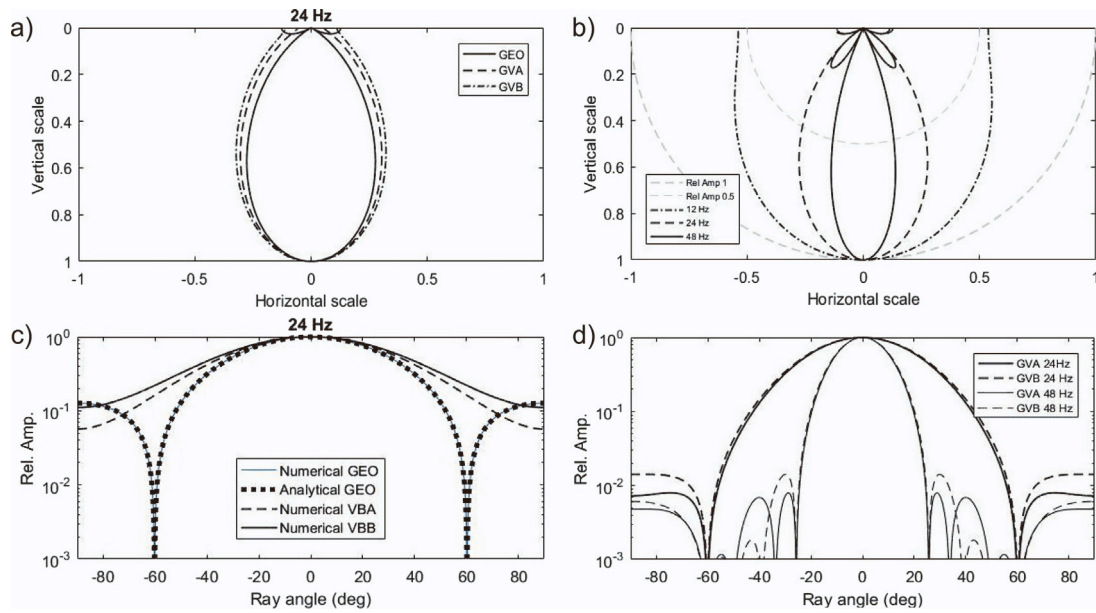

Fig. A.1. Scheme of the plane harmonic wave with wavefront W, frequency f, propagation velocity V, wavelength $\lambda = V/f$, ray angle α. The signal with apparent wavelength $\lambda_a = \lambda/sin\alpha$ is sampled with weights $w(i)$ ($i = 1, \ldots, N$) by the array disposed with regular spacing Δx and central point i_c.

Fig. A.2. Diagrams and responses of the geophone and vibrator arrays. (a) Plot of polar radiation diagrams calculated for geophone, vibrator configuration A (VIB A), vibrator configuration B (VIB B) at the harmonic frequency 24 Hz. (b) Polar plots of the geophone array diagrams calculated at the harmonic frequencies 12, 24, 48 Hz. (c) Array response vs ray angle α (emission or incidence), showing the geophone numerical response, the geophone analytical response together with the VIB A, VIB B responses calculated at 24 Hz. (d) Composition of geophone and vibrator (GVA and GVB in vibrator configuration A and B, respectively) array's responses vs ray angle α, for plane harmonic waves at frequencies 24 and 48 Hz.
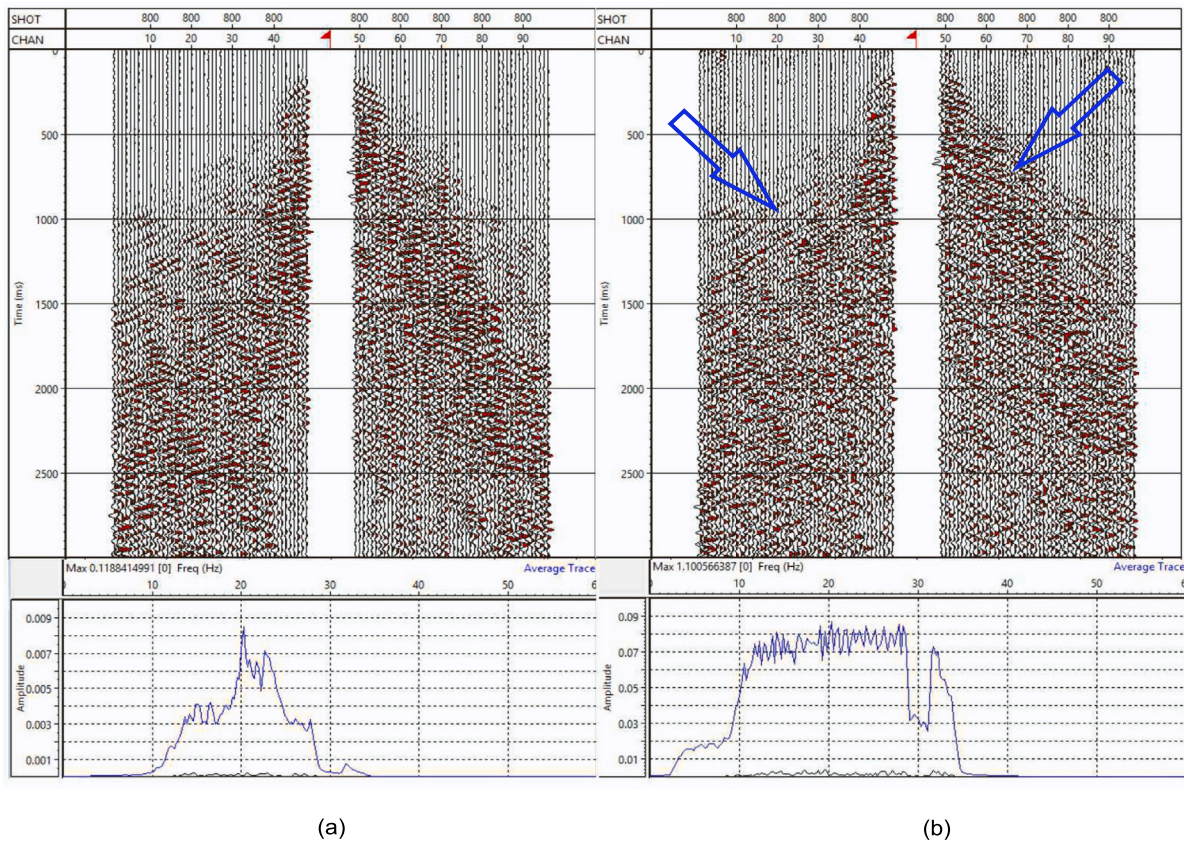
Fig. B.1. Common-shot time gathers (upper) and averaged frequency spectra (lower) of a Los Humeros record (a) before and (b) after signal deconvolution (SP 800 - line L4). The arrows show the improvement in the seismic signal.

the composition of the geophone and vibrator curves for the signals with 12, 24, and 48 Hz frequencies. In Fig. A.2d the receiver and

source signals are composed assuming equal emission and emergence ray angles, respectively. The notch at 60 deg for the signal of frequency
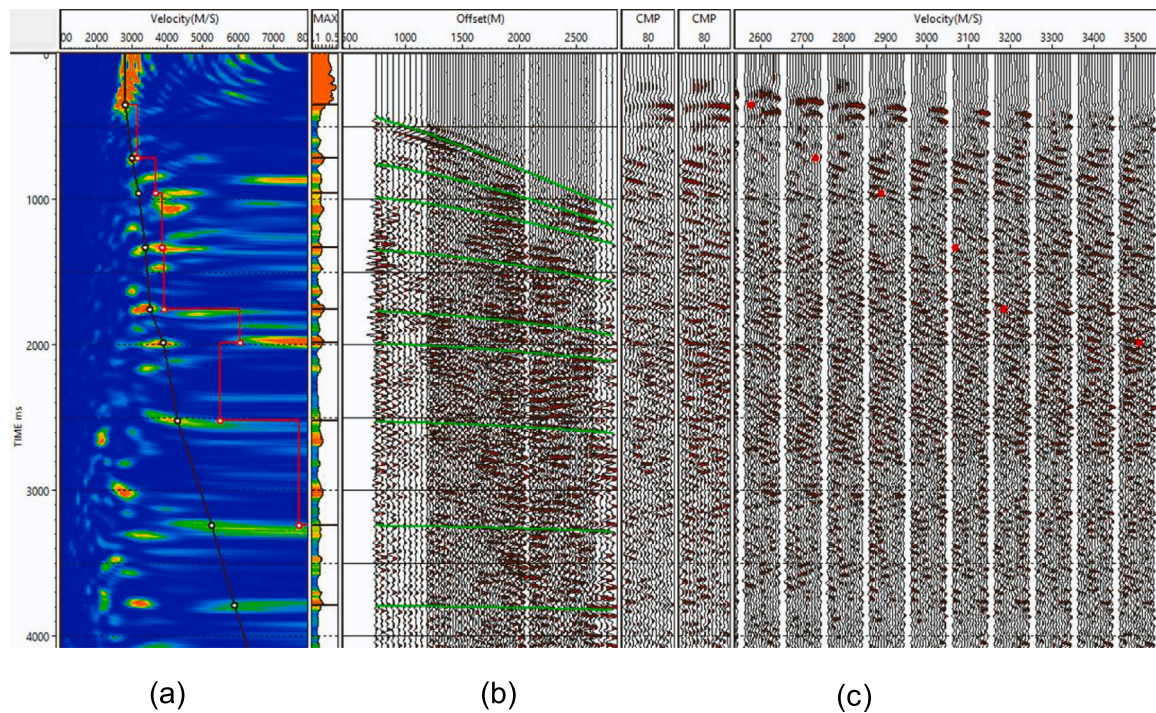
Fig. B.2. Stacking velocity analysis, with (a) semblance, the black line indicates the picked velocity, the red line is the corresponding interval velocity, (b) CMP versus offset gather, the green lines highlight the reflections corresponding to the picked velocity, (c) common velocity stacks, the red dots are the projections on the picked velocities on the stacks. (For interpretation of the references to color in this figure legend, the reader is referred to the web version of this article.)

24 Hz can be observed also in figures (a), (b) and (c). The plots confirm the importance of the evaluation of the directional effects of the acquisition layout for seismic waves also at relatively low frequency in the context of this survey. Even more evident, in this example we can observe the significant directional effect of the source-receiver acquisition layout.

Appendix B. Time processing parameters

Taking into account the source patterns/geophones arrays directional filtering action, explained in Section 3.2, which mask the high-frequency source-induced noise, we applied a restricted zero-phase pass-band filter 4-8-30–35 Hz, to remove high frequency noise attributed to the arrays of operating vibrator sources. Then we applied a spiking deconvolution with operator length 800 ms, and pre-whitening noise 5%. The main purpose of deconvolution was to reduce overall signal ringing, with presence of colored components, and improve the subsequent velocity analysis in this complex area, where the presence of coherent refracted, scattered and converted events sometimes makes it difficult to focus on the reflection events. Fig. B.1 shows the improvement in the signal amplitude and in the amplitude vs frequency distribution in the selected bandwidth operated by the spiking deconvolution.

The next step was the constant velocity stack analysis that we calculated through the combined iteration of the constant velocity stack (CVS) panel, offset sort record and semblance analysis, calculated about every 10 common depth point (CDP), i.e. 250 m, along the seismic lines, as shown in the example of Fig. B.2.

References

Accaino, F., Böhm, G., Tinivella, U., 2005. Tomographic inversion of common image gathers. First Break 23 (3), http://dx.doi.org/10.3997/1365-2397.2005006.

Aragón-Aguilar, A., Izquierdo-Montalvo, G., López-Blanco, S., Arellano-Gómez, V., 2017. Analysis of heterogeneous characteristics in a geothermal area with low permeability and high temperature. Geosci. Front. 8, 1039–1050.

Arzate, J., Corbo-Camargo, F., Carrasco-Núñez, G., Hernández, J., Yutsis, V., 2018. The Los Humeros (Mexico) geothermal field model deduced from new geophysical and geological data. Geothermics 71, 200–211.

Bakulin, A., Golikov, P., Dmitriev, M., Neklyudov, D., Leger, P., Dolgov, V., 2018. Application of supergrouping to enhance 3D prestack seismic data from a desert environment. Lead. Edge 16, 2–240. http://dx.doi.org/10.1190/tle37030200.1.

Bakulin, A., Silvestrov, I., Aldawood, A., Hemyari, E., Poletto, F., 2020. Processing and analysis of seismic-while drilling data acquired with wireless geophones and instrumented top drive in the desert environment. In: Expanded Abstracts, SEG International Exposition and 90th Annual Meeting. pp. 435–439. http://dx.doi.org/10.1190/segam2020-3425221.1.

Barison, E., Poletto, F., Farina, B., 2019. Offset-gap compensation by seismic interferometry for shallow sig-nals of active-seismic lines acquired in a superhot-geothermal field. In: 1st Conference on Geophysics for Geothermal and Renewable Energy Storage, 9-11/09/19 the Hague, NL. Extended Abstract. http://dx.doi.org/10.3997/2214-4609.201902516.

Berkhout, A.J., Verschuur, D.J., 2009. Integrated imaging with active and passive seismic data. In: 2009 SEG Annual Meeting. Houston, Texas, 2009.

Böhm, G., OGS research group, 2016. Cat3d. In: Computer Aided Tomography for 3-D Models. User Manual. OGS.

Böhm, G., Poletto, F., Barison, E., 2019. Near-surface geophysical investigation for characterization of a vol-canic geothermal reservoir by active-seismic-data tomography and attenuation. In: 1st Conference on Geo-Physics for Geothermal and Renewable Energy Storage, 9-11/09/19 the Hague, NL. Extended Abstract. http://dx.doi.org/10.3997/2214-4609.201902519.

Bonini, M., Maestrelli, D., Corti, G., Del Ventisette, C., Moratti, G., Carrasco-Núñez, G., Giordano, G., Lucci, F., Norini, G., Piccardi, L., Urbani, S., Montanari, D., 2021. Modelling intra-caldera resurgence settings: Laboratory experiments with application to the Los Humeros Volcanic Complex (Mexico). J. Geophys. Res. Solid Earth 126, e2020JB020438. http://dx.doi.org/10.1029/2020JB020438.

Brune, R.H., Yates, M., Liner, C., Bell, L., 2013. Evaluating vibrator spacing including mutual admittance interaction effects. In: Expanded Abstracts. Paper Presented at the 2013 SEG Annual Meeting. Houston, Texas, Paper Number: SEG-2013-0567, pp. 136–140. http://dx.doi.org/10.1190/segam2013-0567.1.

Calcagno, P., Evanno, G., Trumpy, E., Gutiérrez-Negrín, L.C., Macías, J.L., Carrasco-Núñez, G., Liotta, D., 2018. Preliminary 3-D geological models of Los Humeros and Acoculco geothermal fields (Mexico) – H2020 GEMex project. Adv. Geosci. 45, 321–333.

Calcagno, P., Trumpy, E., Gutiérrez-Negrín, L.C., Liotta, D., 2022. A collection of 3D geomodels of the Los Humeros and Acoculco geothermal systems (Mexico). Sci. Data 9, 280. http://dx.doi.org/10.1038/s41597-022-01327-0.

Canales, L.L., 1984. Random noise reduction. In: 54th Annual SEG Meeting. Atlant, http://dx.doi.org/10.1190/1.1894168.

Carrasco-Núñez, G., Arzate, J., Bernal, J.P., Carrera, J., Cedillo, F., Dávila-Harris, P., Hernàndez, J., Hurwitz, S., Lermo, J., Levresse, G., Lòpez, P., Manea, V., Norini, G., Santoyo, E., Willcox, C., 2015. A new geothermal exploration program at los humeros volcanic and geothermal field (Eastern Mexican Volcanic Belt). In: Proceedings World Geothermal Congress. 2015 Melbourne, Australia 19-25 April 2015.

Carrasco-Núñez, G., Bernal, J.P., Davila, P., Jicha, B., Giordano, G., Hernández, J., 2018. Reappraisal of Los Humeros volcanic complex by new U/Th zircon and 40Ar/39Ar dating: implications for greater geothermal potential. Geochem. Geophys. Geosyst. 19 (1), 132–149.

Carrasco-Núñez, G., Branney, M.J., 2005. Progressive assembly of a massive layer of ignimbrite with a normal-to-reverse compositional zoning: the Zaragoza ignimbrite of central Mexico. Bull. Volcanol. 68 (1), 3–20.

Carrasco-Núñez, G., Hernández, J., De León, L., Dávila, P., Norini, G., Bernal, J.P., Jicha, B., Navarro, M., L'opez-Quiroz, 2017a. Geologic Map of Los Humeros volcanic complex and geothermal field, eastern Trans-Mexican Volcanic Belt Mapa geológico del complejo volcánico Los Humeros y campo geotérmico, sector oriental del Cinturón Volcánico Trans-Mexicano. Terra Digit. 1 (2), 1–11.

Carrasco-Núñez, G., Lòpez-Martínez, M., Hernàndez, J., Vargas, V., 2017b. Subsurface stratigraphy and its correlation with the surficial geology at Los Humeros geothermal field eastern Trans-Mexican volcanic belt. Geothermics 67, 1–17.

Carrasco-Núñez, G., McCurry, M., Branney, M.J., Norry, M., Willcox, C., 2012. Complex magma mixing, mingling and withdrawal associated with an intra-Plinian ignimbrite eruption at a large silicic caldera volcano: Los Humeros of central Mexico. GSA Bull. 124 (11/12), 1793–1809.

Cassand, J., Lavergne, M., 1971. Seismic emission by vibrators. In: Seismic Filtering. Society of Exploration Geophysicists. Trans. of Editions Technip, Paris.

Cavazos-Álvarez, J.A., Carrasco-Núñez, G., 2020. Anatomy of the Xáltipan ignimbrite at Los Humeros Volcanic complex; the largest eruption of the Trans-Mexican Volcanic Belt. J. Volcanol. Geotherm. Res. 392, 106755.

COMESA (Compañia Mexicana de Exploraciones S.A.), 1998. Informe Sismologico Final (Vibrosismo) - Area Los Humeros. Los Humeros Sismica2D, Prospecto, p. 201.

Contreras, E., Domía nguez, B., Rivera, O., 1990. Petrophysical mesurements in drill cores from the Los Humeros geothermal field. Geotermia 6 (1), 7–42.

Deb, P., Giordano, G., Shi, X., Lucci, F., Clauser, C., 2021. An approach to reconstruct the thermal history in active magmatic systems: Implications for the Los Humeros volcanic complex, Mexico. Geothermics 96, 102162.

Farina, B., Poletto, F., Mendrinos, D., Carcione, J.M., Karytsas, C., 2019. Seismic properties in conductive and convective hot and super-hot geothermal systems. Geothermics 82, 16–33.

Ferriz, H., Mahood, G.A., 1984. Eruption rates and compositional trends at Los Humeros Volcanic Center Puebla, Mexico. J. Geophys. Res. 89, 8511–8524.

García-Estrada, G.H., 1992. Study for the development of new interpretative criteria for gravity studies of geothermal areas – case study of Los Humeros, Pue., Mexico. Geothermal Res. Coun. Trans. 16, 227–232.

Gashawbeza, E., Lerch, D.W., Wilson, C.K., Klemperer, S.L., Miller, E.L., 2005. Integrated passive and active source seismic investigation of the Northwestern Basin and range province. In: American Geophysical Union, Fall Meeting. 2005 abstract id. S41A-0973.

Geldart, L.P., Sheriff, R.E., 2004. Problems in Exploration Seismology and their Solutions:Chapter 8. In: Geophysical References Series No. 14, SEG Online Store, ISBN: 9781560801153, pp. 253–294. http://dx.doi.org/10.1190/1.9781560801733.

GEMex, 2016. H2020 project: GEMex: Cooperation in Geothermal energy research Europe-Mexico for development of Enhanced Geothermal Systems and Superhot Geothermal Systems. pp. 2016–2020, European Union's Horizon 2020 research and innovation programme under grant agreement No. 727550.

GEMex project, 2019-2020. Deliverables. http://www.gemex-h2020.eu/index.php?option=com_content&view=article&id=12&Itemid=114&lang=en.

Granados-Chavarría, I., Calò, M., Figueroa-Soto, A., Jousset, P., 2022. Seismic imaging of the magmatic plumbing system and geothermal reservoir of the Los Humeros caldera (Mexico) using anisotropic shear wave models. J. Volcanol. Geotherm. Res. 421, 107441. http://dx.doi.org/10.1016/j.jvolgeores.2021.107441.

Gutiérrez-Negrín, L.C.A., 2019. Current status of geothermal-electric production in Mexico. IOP Conf. Ser. Earth Environ. Sci. 249 (1), 012017.

Gutiérrez-Negrín, L.C.A., Izquierdo-Montalvo, G., 2010. Review and update of the main features of the Los Humeros geothermal field, Mexico. In: Proceedings World Geothermal Congress. Bali, Indonesia.

Lermo, J., Antayhua, Y., Quintanar, L., Lorenzo, C., 2008. Estudio sismológico del campo geotérmico de Los Humeros, Puebla, México. Parte I: Sismicidad, mecanismos de fuente y distribución de esfuerzos. Geotermia 21 (1), 25–41.

Levander, A.R., 1988. Fourth-order finite-difference P-SV seismograms. Geophysics 53 (11), 1425–1436.

Lucci, F., Carrasco-Núñez, G., Rossetti, F., Theye, T., White, J.C., Urbani, S., Hossein, A., Y, Asahara., Giordano, G., 2020. Anatomy of the magmatic plumbing system of Los Humeros Caldera (Mexico): implications for geothermal systems. Solid Earth 11 (1), 125–159.

Norini, G., Carrasco-Núñez, G., Corbo-Camargo, F., Lermo, J., Rojas, J.H., Castro, C., Bonini, M., Montanari, D., Corti, G., Moratti, G., Piccardi, L., Chavez, G., Zuluaga, M.C., Ramirez, M., Cedillo, F., 2019. The structural architecture of the Los Humeros volcanic complex and geothermal field. J. Volcanol. Geotherm. Res. 381, 312–329.

Norini, G., Groppelli, G., 2020. Comment on estimating the depth and evolution of intrusions at resurgent calderas: Los Humeros (Mexico) by Urbani, et al.. Solid Earth 11, 2549–2556. http://dx.doi.org/10.5194/se-11-(2020)2549-2020.

Norini, G., Groppelli, G., Sulpizio, R., Carrasco-Núñez, G., Dávila-Harris, P., Pellici-oli, C., Zucca, F., De Franco, R., 2015. Structural analysis and thermal remote sensing of the Los Humeros Volcanic Complex: applications for volcano structure and geothermal exploration. J. Volcanol. Geotherm. Res. 301, 221–237.

Poletto, F., Farina, B., Carcione, J.M., Pinna, G., 2019. Analysis of seismic wave propagation in geothermal reservoirs. In: European Geothermal Congress. Den Haag, The Netherlands, 11-14 June 2019.

Prol-Ledesma, R.M., 1998. Pre- and post-exploitation variations in hydrothermal activity in Los Humeros geothermal field Mexico. J. Volcanol. Geotherm. Res. 83, 313–333.

Pulido, C.L., 2008. Borehole Geophysics and Geology of Well H-43 Los Humeros Geothermal Field, Puebla, Mexico. Report 23, Geothermal Training Program, United Nations University, Iceland.

Toledo, T., Gaucher, E., Jousset, P., Jentsch, A., Haberland, C., Maurer, H., Krawczyk, C., Calò, M., Figueroa, A., 2020. Local Earthquake Tomography at Los Humeros Geothermal Field (Mexico). JGR Solid Earth online publication, http://dx.doi.org/10.1029/2020JB020390.

Urban, E., Lermo, J.F., 2013. Local seismicity in the exploration of Los Humeros geothermal fields, Mexico. In: 38st Workshop on Geothermal Reservoir Engineering. Stanford University, Stanford, California.

Urban, E., Lermo, J.F., 2017. Fracture and stress evaluation using well logs and microseismicity, in the exploitation of Los Humeros geothermal field, Mexico. GRC Trans. 41.

Urbani, S., Giordano, G., Lucci, F., Rossetti, F., Acocella, V., Carrasco-Núñez, G., 2020. Estimating the depth and evolution of intrusions at resurgent calderas: Los Humeros (Mexico). Solid Earth 11 (2), 527–545.

Urbani, S., Giordano, G., Lucci, F., Rossetti, F., Acocella, V., Carrasco-Núñez, G., 2021. Structural studies in active caldera geothermal systems. Reply to comment on estimating the depth and evolution of intrusions at resurgent calderas: Los Humeros (mexico) by Norini and Groppelli (2020). Solid Earth Discussion Paper, MS No.: se-2020-218.

Verma, M.P., Verma, S.P., Sanvicente, H., 1990. Temperature field simulation with stratification model of magma chamber under Los Humeros caldera, Puebla, Mexico. Geothermics 19 (2), 187–197.

Vesnaver, A., Böhm, G., 2000. Staggered or adapted grids for seismic tomography? Lead. Edge 9, 944–950. http://dx.doi.org/10.1190/1.1438762.

Viggiano-G., J.C., Robles, J., 1988. Mineralogía hidrotermal en el campo geotérmico de Los Humeros, Características geoquímicas de las rocas, Los Humeros Pue. II: Geometría del yacimiento. Geotermia. Rev. Mex. Geoen 4, 29–40.

Weydt, L.M., Ramírez-Guzmán, Á.A., Pola, A., Lepillier, B., Kummerow, J., Mandrone, G., Comina, C., Deb, P., Norini, G., Gonzalez-Partida, E., Ramón Avellán, D., Macías, J.L., Bär, K., Sass, I., 2021. Petrophysical and mechanical rock property database of the Los Humeros and Acoculco geothermal fields (Mexico). Earth Syst. Sci. Data 13 (2), 571–598.

Willis, M.E., 2022. Distributed Acoustic Sensing for Seismic Measurements - What Geophysicists and Engineers Need to Know. In: Distinguished Instructor Series, No. 25, Society of Exploration Geophysicists, ISBN: 978-1-56080-384-3.

Yáñez, C., García, S., 1982. Exploración de la región geotérmica Los Humeros-Las Derrumbadas, Estados de Puebla y Veracruz. Comisión Federal de Electricidad, 96 Internal Report.

Yilmaz, Ö., 2001. Seismic Data Analysis, Vol 1 and Vol 2 Investigations in Geophysics No:10. Society of Exploration Geophysicsts, Tulsa, U.S.A.

Further reading

Löer, K., Toledo, T., Norini, G., Zhang, X., Curtis, A., Saenger, E.H., 2020. Imaging the deep structures of Los Humeros geothermal field, Mexico, using three-component seismic noise beamforming. Seismol. Res. Lett. XX, 1–9. http://dx.doi.org/10.1785/0220200022.